Comparison of CMIP6 Historical Climate Simulations and Future Projected Warming to an Empirical Model of Global Climate

Laura A. McBride[1], Austin P. Hope[2], Timothy P. Canty[2], Brian F. Bennett[2], Walter R. Tribett[2], Ross J. Salawitch[1,2,3]

[1]Department of Chemistry and Biochemistry, University of Maryland College Park, College Park, 20740, USA
[2]Department of Atmospheric and Oceanic Science, University of Maryland College Park, College Park, 20740, USA
[3]Earth System Science Interdisciplinary Center, University of Maryland College Park, College Park, 20740, USA

Correspondence to: Laura McBride (mcbridel@umd.edu)

Abstract.

The sixth phase of the Coupled Model Intercomparison Project (CMIP6) is the latest modeling effort for general circulation models to simulate and project various aspects of climate change. Many of the general circulation models (GCMs) participating in CMIP6 provide archived output that can be used to calculate equilibrium climate sensitivity (ECS) and forecast future temperature change based on emissions scenarios from several Shared Socioeconomic Pathways (SSPs). Here we use our multiple linear regression energy balance model, the Empirical Model of Global Climate (EM-GC), to simulate and project changes in global mean surface temperature (GMST), calculate ECS, and compare to results from the CMIP6 multi-model ensemble. An important aspect of our study is comprehensive analysis of uncertainties due to radiative forcing of climate from tropospheric aerosols (AER RF) in the EM-GC framework. We quantify the attributable anthropogenic warming rate (AAWR) from the climate record using the EM-GC and use AAWR as a metric to determine how well CMIP6 GCMs replicate human-driven global warming over the last forty years. The CMIP6 multi-model ensemble indicates a median value of AAWR over 1975-2014 of 0.221°C/decade (range of 0.151 to 0.299°C/decade; all ranges given here are for 5th and 95th confidence intervals), which is notably faster warming than our median estimate for AAWR of 0.135°C/decade (range of 0.097 to 0.195°C/decade) inferred from analysis of the Hadley Center Climatic Research Unit data record for GMST. Estimates of ECS found using the EM-GC (best estimate 2.01°C; range of 1.12 to 4.12°C) are generally consistent with the range of ECS of 1.5 to 4.5°C given by IPCC's Fifth Assessment Report. The CMIP6 multi-model ensemble exhibits considerably larger values of ECS (median 3.74°C; range of 2.19-5.65°C). The dominant factor in the uncertainty for our empirical determinations of AAWR and ECS is imprecise knowledge of AER RF for the contemporary atmosphere. We calculate the likelihood of achieving the Paris Agreement target (1.5°C) and upper limit (2.0°C) of global warming relative to pre-industrial for seven of the SSPs using both the EM-GC and the CMIP6 multi-model ensemble. In our model framework, SSP1-2.6 is the 1.5°C pathway with a 64.8% probability of limiting warming at this level by the end of century and SSP4-3.4 is the 2.0°C pathway, with a 74.0% probability of achieving the Paris upper limit. These estimates are based on the assumptions that climate feedback has been and will remain constant over time since the prior temperature record can be fit so well assuming constant climate feedback. In addition, we quantify the sensitivity of future warming to the curbing of the current rapid growth of atmospheric methane and show major near-term limits on the future growth of methane are especially important for achievement of the 1.5°C goal of future warming. We also quantify warming scenarios assuming climate feedback will rise over time, a feature common among many CMIP6 GCMs; under this assumption, it becomes more difficult to achieve any specific warming target. Finally, we assess warming projections in terms of future anthropogenic emissions of atmospheric carbon. In our model framework, humans can emit only another 268 ± 91 Gt C after 2019 to have a 66% likelihood of limiting warming to 1.5°C, and another 565 ± 120 Gt C to have the same probability of limiting warming to 2.0°C. Given the estimated emission of 11.7 Gt C per year for 2019 due to combustion of fossil fuels and deforestation, our EM-GC simulations suggest the 1.5°C warming target of the Paris Agreement will not be achieved unless carbon and methane emissions are severely curtailed in the next two decades.

1 Introduction

The goals of the Paris Agreement, negotiated in December of 2015, are to keep global warming below 2.0°C relative to the start of the Industrial Era and pursue efforts to limit global warming to 1.5°C. General circulation models (GCMs) project future temperature change using various evolutions of greenhouse gases and determine the likelihood of achieving the goals of the agreement. Many GCMs are participating in the sixth phase of the Coupled Model Intercomparison Project (CMIP6) to quantify how the models represent different aspects of climate change (Eyring et al., 2016). Having accurate projections of future temperature is critical for achieving the goals of the Paris Agreement. Chapter 11 of IPCC's Fifth Assessment Report shows that some of the previous generations of these models participating in phase 5 of the Coupled Model Intercomparison Project (CMIP5) (Taylor et al., 2012) tended to overestimate the increase in global mean surface temperature (GMST) for the 21st century (Kirtman et al., 2013). In this analysis we use a multiple linear regression energy balance model to quantify the change in GMST from 1850-2019, project future changes in GMST, compare to the CMIP6 multi-model ensemble, and determine the likelihood of achieving the goals of the Paris Agreement.

Several prior studies have used a multiple linear regression approach to model the GMST anomaly in order to quantify the impact of anthropogenic and natural factors on climate (Foster and Rahmstorf, 2011; Lean and Rind, 2008, 2009; Zhou and Tung, 2013). Typically, total solar irradiance, volcanoes, and El Niño southern oscillation (ENSO) are the natural components represented in the multiple linear regression, and greenhouse gases and aerosols are the anthropogenic factors. We use multiple linear regression, in connection with a dynamic ocean module that accounts for the export of heat from the atmosphere to the ocean, to represent the natural and anthropogenic components of the climate system. In addition to the typical natural factors listed above, we include the Atlantic meridional overturning circulation (AMOC), Pacific decadal oscillation (PDO), and Indian Ocean dipole (IOD) to provide a robust representation of the natural climate system (Canty et al., 2013; Hope et al., 2017). Our anthropogenic components also include the effect of land use change (i.e., deforestation) on Earth's albedo and the export of heat from the atmosphere to the ocean as the atmosphere warms.

Our analysis builds on the work of Canty et al. (2013) and Hope et al. (2017) and includes several key updates. One is the extension back in time of our analysis to 1850. The Hadley Center Climatic Research Unit (Morice et al., 2012), Berkley Earth Group (Rohde et al., 2013), and Cowtan and Way (2014) provide GMST records starting in 1850, which now allows for a simulation of GMST that covers 170 years. The second update is the use of the Shared Socioeconomic Pathways (SSPs) (O'Neill et al., 2017) as our climate scenarios to designate future evolution of greenhouse gas and aerosol abundances. The third is the adoption of an upper ocean to our model, formulated in a manner that matches the equations of Bony et al. (2006) and Schwartz (2012). A description of the model, the various input parameters used, and the updates listed above is given in Sect. 2. Section 3 provides results of CMIP6 comparing to the historical climate record, equilibrium climate sensitivity (ECS), as well as comparisons of our model and CMIP6 projections of future GMST change. Discussion of these results is provided in Sect. 4, along with concluding remarks.

2 Data and Methodology

2.1 Empirical model of global climate

In this analysis we use the empirical model of global climate (EM-GC), which provides a multiple linear regression, energy balance simulation of GMST. As detailed in the following paragraphs, the EM-GC solves for ocean heat uptake efficiency (κ) and six regression coefficients to minimize the cost function in Eq. (1).

$$Cost\ Function = \sum_{i=1}^{N_{MONTHS}} \frac{1}{\sigma_{OBSi}^2} (\Delta T_{OBSi} - \Delta T_{MDLi})^2 \qquad (1)$$

In this equation, ΔT_{OBS} represents a time series of observed monthly GMST anomalies, ΔT_{MDL} is the modeled monthly change in GMST, σ_{OBS} is the 1-sigma uncertainty associated with each temperature observation, *i* is the index for each month, and N_{MONTHS} is the total number of months used in the analysis. For this analysis, we trained the model from 1850-2019. The observed GMST anomalies are blended near surface air and sea surface temperature differences relative to the GMST anomaly over 1850-1900, which is assumed to represent pre-industrial conditions.

We consider several anthropogenic and natural factors as components of $\Delta T_{MDL.}$ The radiative forcing (RF) due to greenhouse gases (GHGs), anthropogenic aerosols (AER), land use change (LUC), and the export of heat from the atmosphere to the world's oceans are the anthropogenic components of ΔT_{MDL}. The influence on GMST from total solar irradiance (TSI), El Niño southern oscillation (ENSO), the Atlantic meridional overturning circulation (AMOC), volcanic eruptions that reach the stratosphere and enhance stratospheric aerosol optical depth (SAOD), the Pacific decadal oscillation, (PDO) and the Indian Ocean dipole (IOD) are the natural components of ΔT_{MDL}. Equation (2) shows how we calculate ΔT_{MDL}, the modeled monthly change in GMST.

$$\Delta T_{MDLi} = \frac{1+\gamma}{\lambda_P} \{GHG\ \Delta RF_i + AER\ \Delta RF_i + LUC\ \Delta RF_i - Q_{OCEAN\ i}\} + C_0 + C_1 \times SAOD_{i-6} +$$

$$C_2 \times TSI_{i-1} + C_3 \times ENSO_{i-2} + C_4 \times AMOC_i + C_5 \times PDO_i + C_6 \times IOD_i \qquad (2)$$

In Eq. (2), GHG ΔRF_i , AER ΔRF_i, and LUC ΔRF_i represent monthly time series of the increase in the stratospheric adjusted values of the RF of climate (Solomon, 2007) since 1750. The parameter λ_P represents the response of a blackbody to a perturbation in the absence of climate feedback (3.2 W m^{-2}, (Bony et al., 2006)). The SAOD, TSI, and ENSO are lagged by 6, 1, and 2 months respectively. The lag of 6 months for SAOD is representative of the time needed for the surface temperature to respond to a change in the aerosol loading due to a volcanic eruption (Douglass and Knox, 2005). This lag is the same as used by Lean and Rind (2008) and Foster and Rahmstorf (2011). The 1 month delay for TSI yields the maximum value of C_2, the solar irradiance regression coefficient. Lean and Rind (2008) and Foster and Rahmstorf (2011) also use a 1 month lag for TSI in their analyses. The 2 month delay for the response of GMST to ENSO is the lag needed to obtain the largest value of the correlation coefficient of the Multivariate ENSO Index version 2 (MEI.v2) (Wolter and Timlin, 1993; Zhang et al., 2019) versus the value of T_{ENSO} calculated by Thompson et al. (2009). In Thompson et al. (2009), T_{ENSO} is the simulated response of GMST to variability induced by ENSO, taking into consideration the effective heat capacity of the atmospheric-ocean mixed layer. Lean and Rind (2008) used a 4-month lag for ENSO.

The term $AMOC_i$ represents the influence of the change in the strength of the thermohaline circulation on GMST (Knight et al., 2005; Medhaug and Furevik, 2011; Stouffer et al., 2006; Zhang and Delworth, 2007). We use the Atlantic multidecadal variability, based on the area weighted monthly mean sea surface temperature (SST) in the Atlantic Ocean between the equator and 60°N (Schlesinger and Ramankutty, 1994), as a proxy for the strength of AMOC. A strong AMOC is characterized by northward flow of energy that would otherwise be radiated to space, which occurs in both the ocean and atmosphere and leads to particularly warm summers in Europe (Kavvada et al., 2013) as well as a number of other well documented influences in other climatic regions (Nigam et al., 2011). The total anthropogenic RF of climate is used to detrend the AMOC signal because this method provides a more realistic approach to infer the changes in the strength of AMOC and its effect on GMST than other detrending options (Canty et al., 2013).

The dimensionless parameter γ represents the sensitivity of the global climate to feedbacks that occur due to a change in the RF of GHGs, AER, and LUC. We relate γ to the climate feedback parameter, λ_{Σ}, as shown in Eq. (3).

$$1+\gamma=\frac{1}{1-\left(\frac{\lambda_{\Sigma}}{\lambda_{P}}\right)}$$

$$\text{where } \lambda_{\Sigma} = \Sigma \text{ all climate feedbacks} \qquad (3)$$

$$\text{i.e., } \lambda_{\Sigma} = \lambda_{\text{Water Vapor}} + \lambda_{\text{Lapse Rate}} + \lambda_{\text{Clouds}} + \lambda_{\text{Surface Albedo}}$$

The relation between λ_{Σ} and γ in Eq. (3) is commonly used in the climate modeling community (Sect. 8.6 of Solomon (2007)). Bony et al. (2006) and Gregory (2000) use a different formalism to define their climate feedback parameter. Our value of λ_{Σ} is related to the IPCC's Fifth Assessment Report ((Stocker et al., 2013), hereafter IPCC 2013) definition of λ via $\lambda_{\Sigma} = \lambda_{P} - \lambda$.

Our model explicitly accounts for the export of heat from the atmosphere to the world's oceans (i.e., ocean heat export or OHE). The quantity Q_{OCEAN} in Eq. (2) represents OHE. In our previous analyses (Canty et al., 2013; Hope et al., 2017), Q_{OCEAN} was subtracted outside of the climate feedback multiplicative term $(1+\gamma)/\lambda_{P}$. We have rewritten Eq. (2) to be comparable to the formulation for this term used by Bony et al. (2006) and Schwartz (2012). The effect of this update results in our model being able to fit the historical climate record with higher values of climate feedback, especially for strong aerosol cooling (see Fig. S1 and supplement for more information). We calculate Q_{OCEAN} by simulating the long-term trend in observed ocean heat content (OHC) as shown in Eq. (4) and Eq. (5).

$$Q_{OCEANi} = \kappa\left(\Delta T_{ATM,HUMANi} - \Delta T_{OCEAN,HUMANi}\right) \qquad (4)$$

$$\kappa = \frac{OHE \times \Delta t}{\int_{t_{START}}^{t_{END}}\left(\left[\frac{1+\gamma}{\lambda_P}\{GHG\ RF_{i-72}+AER\ RF_{i-72}+LUC\ RF_{i-72}\}\right]-\left[f_0 \sum_0^{i-72} Q_{OCEAN}\right]\right)dt} \qquad (5)$$

The κ term is the ocean heat uptake efficiency (W m^{-2} $°C^{-1}$) and is based on the definition used in Raper et al. (2002), where κ is the ratio between the atmosphere and ocean temperature difference that best fits observed OHC data (Sect. 2.2.8 describes the OHC data records used in our analysis). The value of κ is determined based upon the best fit (described below) between Q_{OCEAN} and the observed OHC record. The term $\Delta T_{OCEAN,HUMAN}$ represents the temperature response of the well-mixed, top 100 m of the ocean due to the total anthropogenically driven rise in OHC. This formulation of $\Delta T_{OCEAN,HUMAN}$ allows the model ocean to warm in response to an atmospheric warming. We use a 6 year lag (72 months) for Q_{OCEAN} to account for the time needed for the energy leaving the atmosphere to heat the upper ocean and penetrate to depth, based on Schwartz (2012). Our analysis of modeled GMST is insensitive to whether this 6 year lag or the 10 year lag from Lean and Rind (2009) is used. The t_{START} and t_{END} limits on the integral in Eq. (5) are the start and end years, associated with each OHC record. The start and end years vary between the 5 OHC records (see supplement for the different start and end years). The constant f_0 term in Eq. (5) is a combination of the heat capacity of ocean water, the fraction of total ocean volume in the surface layer, and the fraction of total Q_{OCEAN} that warms the surface layer, and is equal to 8.76×10^{-5} °C m^2 W^{-1}. We represent the global ocean as being 1 km deep for 10% of the ocean area (representing the continental shelves) and 4 km deep for the remaining area, which approximates the average depth of the actual world's oceans to within 3%; 3.7 km compared to 3.682-3.814 km from Charette and Smith (2010). Based upon our analysis of decadal ocean warming as a function of depth extracted from CMIP5 GCMs, we have determined that 13.7% of the rise in total OHC occurs in the well mixed, upper 100 m of the ocean, the term represented by $\Delta T_{\mathrm{OCEAN,HUMAN}}$ in equation (4). The bottom rung of Fig. 1 compares our modeled OHC to the observed OHC record based upon the average of five data sets; the value of κ resulting in the best simulation of observed OHC is shown.

We use the reduced chi-squared (χ^2) metric to define the goodness of fit between the modeled and measured GMST anomaly for the atmosphere and also between simulated and observed OHC. Equation (6) and Eq. (7) show the calculations for χ^2 for the atmosphere, and Eq. (8) shows the calculation for χ^2 for the ocean. As noted above, minimization of the difference between the measured and modeled GMST anomaly results in the EM-GC being able to replicate the observed rise in temperature over the past 170 years quite well, as shown in Fig. 1. We have added two additional new features to the model to assure accurate representation of the rise in OHC as well as the rise in GMST since 1940. The first new feature, Eq. (7), was added because of a change in the specification of the uncertainty of the GMST anomaly (σ_{OBSi} in Eq. (2)) given by the Hadley Center Climatic Research Unit (HadCRUT). A recent update resulted in much larger uncertainties being ascribed to the GMST anomaly for the entire data record, which caused some solutions to yield visually poor simulations of the rise in GMST over the past 4 to 5 decades. The second new feature, Eq. (8), was added because for some selections of the radiative forcing due to tropospheric aerosols (AER ΔRF_i in Eq. (2)), the original model formulation was converging but producing simulations of OHC that seemed physically improper, based on visual inspection of observed and modeled OHC. As a result of these two issues, all calculations shown here are subject to three goodness-of-fit constraints, described by Eq. (6) to (8):

$$\chi^2_{ATM} = \frac{1}{N_{YEARS} - N_{FITTING\ PARAMETERS} - 1} * \sum_{j=1}^{N_{YEARS}} \frac{1}{\langle\sigma_{OBSj}\rangle^2} \left(\langle\Delta T_{OBSj}\rangle - \langle\Delta T_{MDLj}\rangle\right)^2 \quad (6)$$

$$\chi^2_{RECENT} = \frac{1}{N_{YEARS,REC} - N_{FITTING\ PARAMETERS} - 1} * \sum_{j=1}^{N_{YEARS,REC}} \frac{1}{\langle\sigma_{OBSj}\rangle^2} \left(\langle\Delta T_{OBSj}\rangle - \langle\Delta T_{MDLj}\rangle\right)^2 \quad (7)$$

$$\chi^2_{OCEAN} = \frac{1}{N_{YEARS} - N_{FITTING\ PARAMETERS} - 1} * \sum_{j=1}^{N_{YEARS,OHC}} \frac{1}{\langle\sigma_{OBSj}\rangle^2} \left(\langle OHC_{OBSj}\rangle - \langle OHC_{MDLj}\rangle\right)^2 \quad (8)$$

Here, $<\Delta T_{OBS}>$, $<\Delta T_{MDL}>$, and $<\sigma_{OBS}>$ in Eq. (6) and Eq. (7) represent the annually averaged observed, modeled, and uncertainty in the GMST anomaly, respectively. The variable $N_{FITTING\ PARAMETERS}$ is equal to 9 for typical simulations, the sum of 7 (the number of regression coefficients) plus 2 (model output parameters γ and κ). In Eq. (8), $<OHC_{OBS}>$ and $<OHC_{MDL}>$ represent the annual averaged observed and modeled OHC. The σ_{OBS} term in Eq. (8) is the uncertainty in the OHC record (see Sect. 2.2.8 for more information). The equation for all three formulations of χ^2 is based on annual averages, rather than monthly time series, because the autocorrelation functions of ΔT_{OBS} and ΔT_{MDL} display similar shapes using annual averages, and do not match utilizing monthly averages (see supplement of Canty et al. (2013) for further explanation). For Eq. (6) to (8), we define an acceptable fit to the climate record as $\chi^2 \leq 2$. The number of years (N_{YEARS}) varies across the three equations. Equation (6) uses the total number of years in the GMST record, which for HadCRUT is 170 years. The number of years in Eq. (8), $N_{YEARS,OHC}$, depends on the OHC data set used, as each data set spans a different range. The average of five OHC data sets that is our primary data source extends from 1955-2017, a total of 63 years. The value of χ^2_{OCEAN} found using Eq. (8) is displayed on the bottom rung of Fig. 1. All model simulations shown throughout this paper have $\chi^2_{OCEAN} \leq 2$, representing a good fit to the observed rise in OHC over the time of the data record.

The calculation of χ^2_{RECENT} shown in Eq. (7) is used to constrain the model to match the observed changes in GMST over the time frame 1940-2019, a total of 80 years ($N_{YEARS,REC}$ equals 80). This time frame was chosen to include a full cycle of AMOC, as the strength of the thermohaline circulation tends to vary on a period of 60-80 years (Chen and Tung, 2018; Kushnir, 1994; Schlesinger and Ramankutty, 1994). As noted above, the χ^2_{RECENT} constraint was added to our model framework because the large temperature uncertainties associated with v4.6 of the HadCRUT data set allowed the original model to provide numerically good fits but poor visual fits to GMST changes in the recent time period (i.e. the red line in the top rung of Fig. 1 starts to strongly deviate from the black line beginning in about 2000 under certain conditions). All model simulations shown below have $\chi^2_{RECENT} \leq 2$ representing a good fit to the

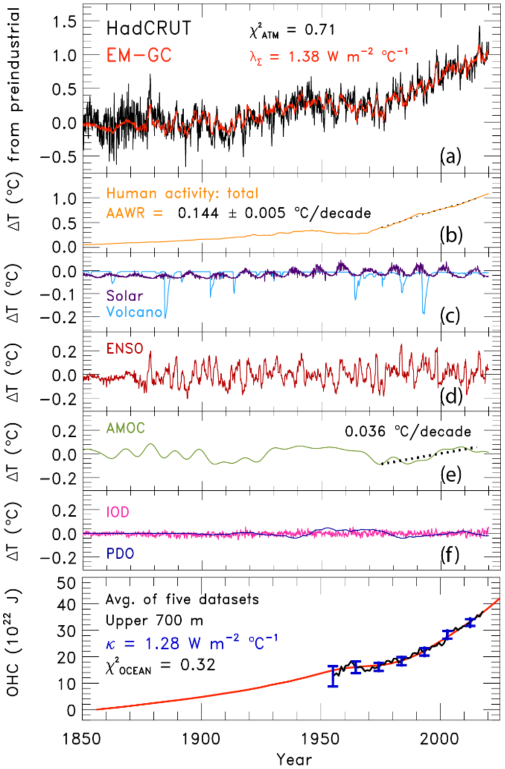

Figure 1. Measured and modeled GMST anomaly (ΔT) relative to a pre-industrial (1850-1900) baseline. (a) Observed (black) and modeled (red) ΔT from 1850-2019. This panel also displays the values of λ_Σ and χ^2_{ATM} (see text) for this best-fit simulation. (b) Contributions from total human activity. This panel also denotes the best estimate numerical value of the attributable anthropogenic warming rate from 1975-2014 (black dashed) as well as the 2σ uncertainty in the slope for a model run that uses the best estimate of AER RF_{2011} of −0.9 W m^{-2}. (c) Solar irradiance (light blue) and major volcanoes (purple). (d) Influences from ENSO on ΔT. (e) Contributions from AMOC to ΔT and to observed warming from 1975-2014. (f) Influences from PDO (blue) and IOD (pink) on ΔT. (g) Measured (black) and modeled (red) ocean heat content (OHC) as a function of time for the average of five data sets (see text), the value of χ^2_{OCEAN} for this run, as well as the ocean heat uptake efficiency, κ, needed to provide the best-fit to the OHC record. The error bars (blue) denote the uncertainty in OHC used in this analysis (see Sect. 2.2.8).

observed rise in GMST over the past 80 years, which results in modeled GMST that replicates observed GMST for the entire time series.

Figure 1 shows the observed (HadCRUT) and modeled GMST anomaly from 1850-2019, and the various anthropogenic and natural components that constitute modeled GMST (see Fig. S3 for results using Cowtan and Way (2014) GMST record and the Cheng et al. (2017) OHC record (hereafter Cheng 2017)). Figure 1a shows the value of climate feedback, 1.38 W m^{-2} $°C^{-1}$, that is needed to achieve a best fit to the climate record for this simulation, resulting in values of $\chi^2_{ATM} = 0.71$ and $\chi^2_{OCEAN} = 0.32$. Figure 1b is the total contribution of human activity to variations in GMST, which includes GHGs, AER, LUC, and the export of heat from the atmosphere to the ocean. For the simulation shown, the aerosol radiative forcing is −0.9 W m^{-2}, the best estimate given by IPCC 2013 (Myhre et al., 2013). This panel also notes the best estimate of the time rate of change of GMST attributed to humans from 1975-2014, or the attributable anthropogenic warming rate (AAWR (see Sect. 2.3)). Figure 1c illustrates the contribution to the GMST anomaly from TSI (Solar) and SAOD (Volcano) over the 170-year period. The influences of ENSO and AMOC are indicated in Figs. 1d and 1e, respectively. The contribution of AMOC to the rise in GMST over 1975-2014 (the same time period used to define AAWR) is also specified on Fig. 1e. Figure 1f indicates the small effect of IOD and PDO on GMST in our model framework. The last panel, Fig. 1g, shows the time series of observed OHC based upon the average of five data sets for the upper 700 m of the ocean (black points and blue error bars; see Sect. 2.2.8) and the modeled value of OHC (red line). For this simulation, the OHC data is best fit for a value of κ equal to 1.28 W m^{-2} $°C^{-1}$, which falls within the range of empirical estimates for this parameter given by Raper et al. (2002). The sum of the contributions of human activity, TSI, SAOD, ENSO, AMOC, PDO and the IOD to temporal variations in the GMST anomaly shown in Fig. 1b to 1f plus the value of C_0 equals the modeled GMST anomaly, shown by the red line in Fig. 1a.

Altering the training period of our model has a slight effect on our results (see Fig. S2 and the supplement for information on various training periods). We project relatively similar results for end of century warming for training periods that start in 1850 and end in either 2009 or 1999, compared to results shown throughout the paper for a training period of 1850 to 2019, indicating the stability of our approach. As detailed in the supplement, we do find some differences from the results shown in the paper upon use of a training period of 1850 to 1989 due to the reduction in the number of years considered from the available OHC records.

2.2 Model Inputs

2.2.1 Temperature data

We use five global mean surface temperature anomalies from the Hadley Centre Climatic Research Unit (HadCRUT, (Morice et al., 2012)) from 1850-2019, National Centers for Environmental Information NOAAGlobalTemp v5 (NOAAGT, (Smith et al., 2008; Zhang et al., 2019)) from 1880-2019, NASA Goddard Institute of Space Studies Surface Temperature Analysis v4 (GISTEMP, (Hansen et al., 2010)) from 1880-2019, Berkeley Earth Group (BEG, (Rohde et al., 2013)) from 1850-2019, and Cowtan and Way (2014) (CW14; see Fig. S4 and the supplement for information on CW14 GMST record) from 1850-2019. Our analysis primarily uses the HadCRUT GMST data set, because this GMST record is the central focus of some contemporary studies (Liang et al., 2020; Nicholls et al., 2020a, 2020b), but in some sections, results are shown for all five data sets. All temperature anomalies are with respect to a pre-industrial baseline (1850-1900). To alter each data record so that the temperature anomaly is relative to the same pre-industrial baseline, we adjust all data sets relative to the HadCRUT baseline of 1961-1990 because we primarily use the HadCRUT data record in this analysis. We then adjust each data set to the pre-industrial baseline, as described in the methods section of Hope et al. (2017).

2.2.2 Shared Socioeconomic Pathways

For this analysis, we use the estimates of the future abundances of greenhouse gases and aerosols provided by the SSPs. There are twenty-six scenarios, five baseline pathways and twenty-one mitigation scenarios. The baseline pathways follow specific narratives for factors such as population, education, economic growth, and technological developments of sources of renewable energy (Calvin et al., 2017; Fricko et al., 2017; Fujimori et al., 2017; Kriegler et al., 2017; van Vuuren et al., 2017) to represent several possible futures spanning different challenges for adaptation and mitigation to climate change as illustrated in Fig. 1 of O’Neill et al. (2014). The twenty-one mitigation scenarios follow one of the baseline pathways but include specific climate policy to reach a designated radiative forcing at the end of the century.

As part of CMIP6, the ScenarioMIP experiment (O'Neill et al., 2016) includes eight SSPs (SSP1-1.9, SSP1-2.6, SSP4-3.4, SSP2-4.5, SSP4-6.0, SSP3-7.0, SSP5-8.5, and SSP5-3.4-OS) that GCMs use to project future GMST. The first number is the reference pathway that the scenario follows (i.e. SSP1 follows the first SSP narrative) and the numbers after the dash are the target radiative forcing at the end of the century (i.e. SSP1-2.6 reaches around 2.6 W m^{-2} in 2100). The ScenarioMIP experiment designates Tier 1 and Tier 2 scenarios. The Tier 1 scenarios are SSP1-2.6, SSP2-4.5, SSP3-7.0, and SSP5-8.5 , and the Tier 2 scenarios are SSP1-1.9, SSP4-3.4, SSP4-6.0, and SSP5-3.4-OS (an overshoot pathway that follows SSP5-8.5 until around 2040, where carbon dioxide emissions drastically decrease and become negative in 2065). Our analysis includes seven of the eight ScenarioMIP SSPs: all but the overshoot pathway. We highlight four in the main paper: two Tier 1 (SSP1-2.6 and SSP2-4.5) and two Tier 2 (SSP1-1.9 and SSP4-3.4) scenarios. Analysis of the other three SSPs is included in the supplement. Figure 2 shows the time evolution of the atmospheric abundance of the three major anthropogenic GHGs (carbon dioxide, methane, and nitrous oxide) for each of the seven SSPs we consider as well as observations of the global mean atmospheric abundance for these gases to the end of 2019 (Dlugokencky, 2020; Dlugokencky and Tans, 2020).

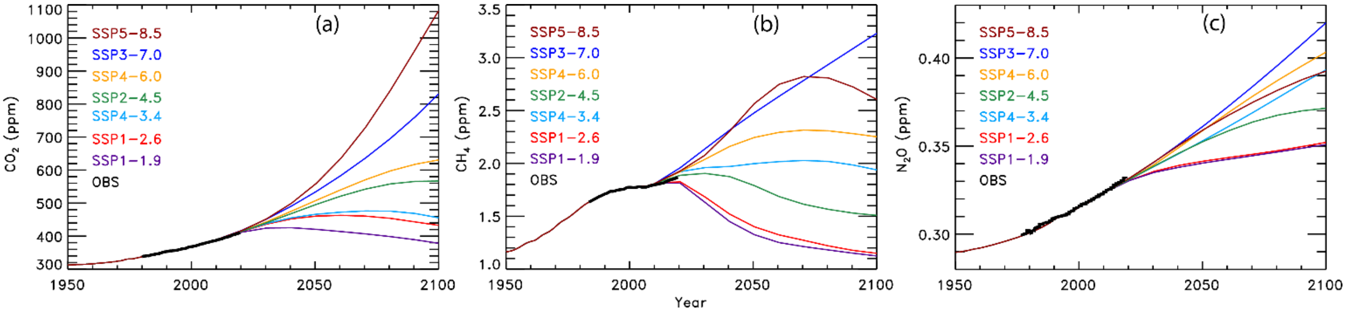

Figure 2. Observed and projected greenhouse gas mixing ratios. (a) Carbon dioxide abundances from observations (black) and seven of the ScenarioMIP SSPs (colors, as indicated). (b) Methane abundances from observations and ScenarioMIP SSPs. (c) Nitrous oxide abundances from observations and ScenarioMIP SSPs.

2.2.3 Greenhouse gases

The historical values of GHG mixing ratios were provided by Meinshausen et al. (2017) from 1850-2014. We used the equations from Myhre (1998) to calculate the change in RF due to carbon dioxide (CO_2), methane (CH_4), nitrous oxide (N_2O), ozone depleting substances (ODS), hydrofluorocarbons, perfluorocarbons, and sulfur hexafluoride relative to RF in year 1850. We also used the updated pre-industrial values of CH_4 and N_2O from IPCC 2013 and the radiative efficiencies from WMO (2018) The radiative forcing of CH_4 also includes the 15% enhancement from the increase in stratospheric water vapor due to rising atmospheric CH_4 (Myhre et al., 2007). Values of GHG mixing ratios, other than ODSs, from 2015-2100 are from the SSP Database (Calvin et al., 2017; Fricko et al., 2017; Fujimori et al., 2017; Kriegler et al., 2017; Rogelj et al., 2018; van Vuuren et al., 2017) and are provided on a decadal basis. These mixing ratios were interpolated onto a monthly time scale. We used the estimates of future ODS abundances provided in Table 6-4 of the 2018 Ozone Assessment Report (Carpenter et al., 2018), because the SSP database did not provide these estimates. We also include tropospheric ozone (O_3^{TROP}) as a GHG, because tropospheric ozone rivals N_2O as the third most important anthropogenic GHG (Fig 8.15 of Myhre et al. (2013)). The RF due to O_3^{TROP} from the RCPs provided by the Potsdam Institute for Climate Impact Research (Meinshausen et al., 2011) is used, because the SSP database does not provide estimates. Values of RF due to O_3^{TROP} from RCP2.6, RCP4.5, RCP6.0, and RCP8.5 are substituted in for SSP1-2.6, SSP2-4.5, SSP4-6.0, and SSP5-8.5, respectively. We created new time series for the RF due to O_3^{TROP} for SSP4-3.4 and SSP3-7.0 using linear combinations of RF time series from RCP2.6 and RCP8.5, with weights based on the end of century total RF value due to all GHGs of the respective time series. Finally, the RF time series for O_3^{TROP} from RCP2.6 was also used for SSP1-1.9. Figure S5 shows the ozone RF time series used in this analysis and the supplement provides more information about the creation of the time series for the RF due to O_3^{TROP}.

2.2.4 Aerosol radiative forcing

The value of the change in total aerosol radiative forcing in 2011 relative to pre-industrial (AER RF_{2011}) is highly uncertain. Chapter 8 of the IPCC 2013 report gives a best estimate of AER RF_{2011} as −0.9 W m^{-2}, a likely range between −0.4 and −1.5 W m^{-2}, and a 5th to 95th percent confidence interval between −0.1 and − 1.9 W m^{-2} (Myhre et al., 2013). This substantial range in AER RF_{2011} results in a large spread in future projections of global GMST. Figure 3 shows the effect of varying the value of AER RF_{2011} on projections of GMST in our EM-GC framework, for the same SSP4-3.4 GHG scenario. The middle panel on Figs. 3a, 3b, and 3c shows the contribution to GMST of GHGs, LUC, AER, as well as net human activities. As the value of AER RF$_{2011}$ decreases and aerosols cool more strongly, the value of climate feedback (model parameter λ_Σ) rises, and the net contribution of human impact on GMST by the end of the century increases. Depending on which value of AER RF$_{2011}$ is used, the rise in GMST by year 2100 for the SSP4-3.4 pathway could range from 1.3°C (Fig. 3a) to 2.6°C (Fig. 3c) relative to pre-industrial. Strong aerosol cooling offsets a substantial fraction of GHG-induced warming, and a large value of climate feedback (λ_Σ = 2.32 W m^{-2} °C^{-1}) is needed to fit the historical climate record (Fig. 3c). In this case, future warming is large, well above the goals of the Paris Agreement by the end of the century. Conversely, weak aerosol cooling offsets only a small fraction of GHG-induced warming, resulting in a small value of climate feedback (λ_Σ = 0.73 W m^{-2} °C^{-1}) needed to fit the observed GMST record (Fig. 3a). The use of any of the values of AER RF$_{2011}$ in Fig. 3 can result in a very good fit to the climate record (i.e., $\chi^2_{\mathrm{ATM}} \leq 2$, $\chi^2_{\mathrm{RECENT}} \leq 2$, and $\chi^2_{\mathrm{OCEAN}} \leq 2$).

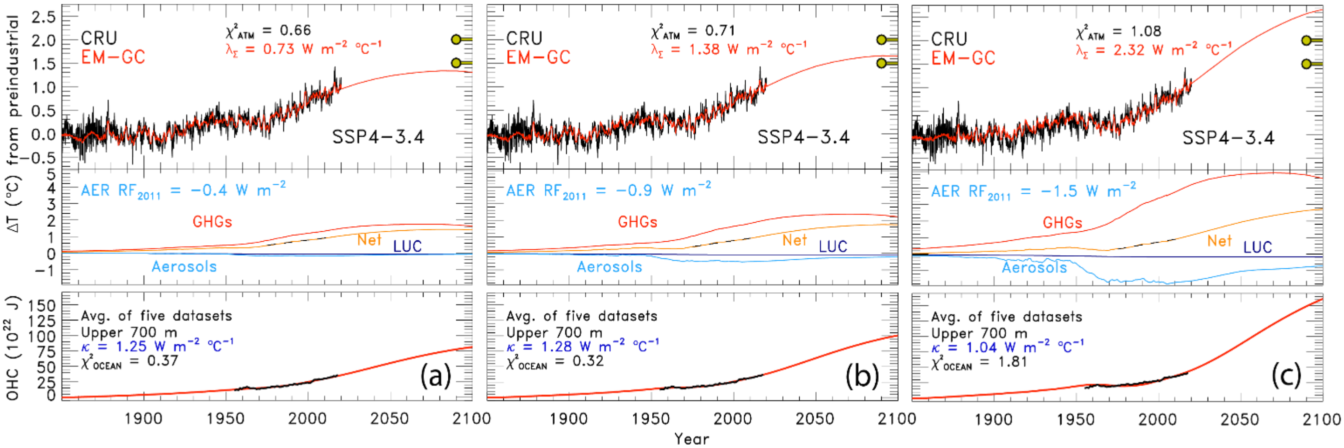

Figure 3. Measured and EM-GC simulated GMST anomaly (ΔT) relative to a pre-industrial (1850-1900) baseline, as well as projected ΔT to end of century for SSP4-3.4. Top panel of each plot displays observed (black) and simulated (red) ΔT, as well as the values of λ_Σ and χ^2_{ATM} for each model run. The Paris Agreement target (1.5°C) and upper limit (2.0°C) are shown (gold circles). The second panel shows the contribution of GHGs, aerosols, and land use change to ΔT, as well as the net human component. The bottom panel compares observed (black) and modeled (red) values of OHC for simulations constrained by the average of five data sets (see text) and also provides the numerical values of κ needed to obtain best-fits to the OHC record as well as best-fit values of χ^2_{OCEAN}. The only difference between (a), (b), and (c) is the time series for RF due to tropospheric aerosols used to constrain the EM-GC; values of AER RF$_{2011}$ for each time series are (a) −0.4 W m^{-2}, (b) −0.9 W m^{-2}, (c) −1.5 W m^{-2}.

We use the total aerosol RF time series provided by the SSP database for each SSP scenario. The database provides AER RF from 2005-2100, with values for all SSPs nearly identical until about 2010 (Riahi et al., 2017; Rogelj et al., 2018). In the EM-GC, we calculate temperature projections over the entire observational period, beginning in 1850. Consequently, we create AER RF time series that begin in 1850 and span the range of uncertainty given by Chapter 8 of IPCC 2013. We use historical estimates of AER RF from 1850-2014 for the four RCPs provided by the Potsdam Institute for Climate Research (Meinshausen et al., 2011). The AER RF value in 2014 from the appropriate historical estimate (i.e. RCP 4.5 is used for SSP2-4.5) is scaled by a constant multiplicative factor, such that the historical RCP value at the end of 2014 matches the SSP time series at the start of 2015, yielding a continuous time series for the RF of climate due to tropospheric aerosols. This scaled time series has AER RF_{2011} nearly equal to -1.0 W m^{-2}, which we take as the SSP-based best estimate of the change in total aerosol radiative forcing in 2011 relative to pre-industrial. Next, the single continuous time series is scaled, again by a constant multiplicative factor, to match the IPCC 2013 best estimate and range of uncertainty for AER RF_{2011} (Myhre et al., 2013). This procedure results in five additional time series of AER RF. Six time series of AER RF are thus created for each SSP, having values of AER RF_{2011} equal to -0.1, -0.4, -0.9, -1.0, -1.5, and -1.9 W m^{-2}. Figure S7 shows these six AER RF time series for SSP1-2.6 and SSP4-3.4. In the EM-GC framework, we further scale these six time series to create a total of 400 AER RF time series to fully analyze the range of AER RF_{2011} given by Myhre et al. (2013).

2.2.5 Total solar irradiance and stratospheric aerosol optical depth

We use the TSI time series provided for the CMIP6 models from 1850-2014 (Matthes et al., 2017) and append values from the Solar Radiation and Climate Experiment (SORCE) (Dudok de Wit et al., 2017) for 2015 to the end of 2019. The values of TSI_i used in Eq. (2) are differences of monthly mean values minus the long-term average (i.e., TSI anomalies). Consistent with prior studies (e.g., Lean and Rind (2008) and Foster and Rahmstorf (2011)) variations in solar irradiance due to the 11-year solar cycle have a small but noticeable effect on the EM-GC simulation of the GMST anomaly (Fig. 1c). For projections of future warming, we set the term TSI_i in Eq. (2) equal to zero from the start of 2020 until 2100 (i.e., we do not propagate 11-year variations of TSI forward in time).

The time series for SAOD is a combination of values computed from extinction coefficients for the CMIP6 GCMs (Arfeuille et al., 2014) from 1850-1978 and the Global Space-based Stratospheric Aerosol Climatology (GloSSAC v2.0) (Thomason et al., 2018) from 1979-2018. Extinction coefficients at 550 nm were integrated from the tropopause to 39.5 km and averaged over the globe using a cosine of latitude weighting. The CMIP6 and GloSSAC extinction coefficients span 80°S to 80°N. To extend the SAOD time series to the end of 2019, we use the level 3, gridded SAOD product from the Cloud-Aerosol Lidar and Infrared Pathfinder Satellite Observations (CALIPSO) (Vaughan et al., 2004). Time series of globally averaged SAOD from CALIPSO have a very similar shape to the GloSSAC time series over the period of overlap (2006-2018), with a slight offset. To append the CALIPSO SAOD for 2018-2019, we took the average difference between the two time series for the overlapping months and then adjusted the CALIPSO time series by this offset. This slight adjustment to the CALIPSO record has no bearing on our scientific results, since the effect of volcanic activity on GMST has been small over the past 2 decades (Fig. 1c). We set the term $SAOD_i$ in Eq. (2) equal to the value in December 2019 from the start of 2020 until 2100.

2.2.6 El Niño southern oscillation, Pacific decadal oscillation, and Indian Ocean dipole

We use the MEI.v2 (Wolter and Timlin, 1993; Zhang et al., 2019) to characterize the influence of ENSO on GMST. In order to obtain a time series that spans the entire training period of our model, 1850-2019, we append three time series to create an MEI.v2 index over the full time extent of our model training period. The MEI.v2 provides two month averages of empirical orthogonal functions of five different climatic variables from 1979 to present (Zhang et al., 2019). To have the ENSO index extend back to 1850, we compute differences in SST anomalies over the tropical Pacific basin as defined by the MEI.v2 from 1850-1870 using HadSST3 (Kennedy et al., 2011). Our internal computation of this surrogate for the MEI index is then appended to the MEI.ext of Wolter and Timlin (2011), which extends from 1871-1978, and the MEI.v2 index of (Zhang et al., 2019) (1979-2019). This full time series provides a representation of ENSO that covers from 1850 to present. Consistent with prior regression-based approaches (Foster and Rahmstorf, 2011; Lean and Rind, 2008), we find a significant portion of the monthly and at times annual variation in GMST is well explained by ENSO (Fig. 1d). As for the other natural terms, we assume $ENSO_i$ in Eq. (2) is zero for 2020-2100.

The Pacific decadal oscillation is the leading principal component of North Pacific monthly SST variability poleward of 20°N (Barnett et al., 1999). The PDO index maintained by the University of

Washington provides monthly values from 1900-2018. The PDO varies on a multidecadal time scale and affects climate in the North Pacific and North America, and has secondary effects in the tropics (Barnett et al., 1999). In our model framework, the expression of PDO on GMST is dependent on the model specification of the AER RF time series, as shown in Fig. S6. At low values of AER RF_{2011}, such as −0.1 W m^{-2}, the effect of PDO on GMST is negligible and the contribution from AMOC dominates. At high values of AER RF_{2011} (−1.5 W m^{-2}), the effect of PDO on GMST is equal to the contribution from AMOC. At high values of AER RF_{2011}, we obtain results similar to findings from England et al. (2014) and Trenberth and Fasullo (2013) that shows the PDO exhibits an appreciable influence on GMST, especially for the 2000-2010 time period.

The Indian Ocean dipole is based upon the difference in the anomalous sea surface temperatures (SST) between the western equatorial Indian Ocean (50°-70° E and 10° S-10° N) and the south eastern equatorial Indian Ocean (90° E-110° E & 10° S-0° N) as defined in Saji et al. (1999). We use 1° × 1° SSTs from the Centennial in situ Observation-Based Estimate (COBE) (Ishii et al., 2005) to create an IOD index from 1850-2019. As noted above and shown on Fig. 1f, the regression coefficients for PDO and IOD are quite small. We find little influence of either PDO or IOD in the HadCRUT time series of GMST, but these terms are retained for completeness. We assume PDO_i and IOD_i in Eq. (2) are zero after the start of 2019 and 2020, respectively.

2.2.7 Atlantic meridional overturning circulation

We use the Atlantic multidecadal variability (AMV) index as the area weighted, monthly mean SST from HadSST3 (Kennedy et al., 2011), between the equator and 60° N in the Atlantic Ocean (Schlesinger and Ramankutty, 1994) to characterize the influence of variations in the strength of the AMOC on GMST. The AMV index is detrended using the RF anomaly due to anthropogenic activity over the historical time frame of the analysis, as discussed in Sect. 3.2.3 of Canty et al. (2013), because this detrending option removes the influence of long-term global warming on the AMV index. The detrended AMV index serves as a proxy for variations in the strength of the AMOC (Knight et al., 2005; Medhaug and Furevik, 2011; Zhang and Delworth, 2007), which has particularly noticeable effects on climate in the Northern Hemisphere (Jackson et al., 2015; Kavvada et al., 2013; Nigam et al., 2011). For this analysis, the index has been Fourier filtered to remove frequencies above 9 yr^{-1} to retain only the low frequency, high amplitude component of the thermohaline circulation (Canty et al., 2013). As noted above and shown in Fig. 1, a considerable portion of the long-term variability in GMST is attributed to variations in the strength of AMOC, including about 0.036°C/decade over the 1975-2014 time period. There is considerable debate about the validity of the use of a proxy such as the AMV index as a surrogate for the climatic effects of AMOC that is centered mainly around how much of the variability of the index is either internal (i.e., natural variability) or externally forced (i.e., driven by anthropogenic factors) (Haustein et al., 2019; Knight et al., 2005; Medhaug and Furevik, 2011; Stouffer et al., 2006). We stress, as explained below, none of our scientific conclusions are altered if we neglect AMV as a regression variable.

2.2.8 Ocean heat content records

Ocean heat content data records from five recent and independent papers are used in this study. We utilize OHC data from Balmaseda et al. (2013), Carton et al. (2018), Cheng et al. (2017), Ishii et al. (2017), and Levitus et al. (2012), as well as the average of the records to model the export of heat (OHE) from the atmosphere to the ocean. Figure S8 shows these five OHC records as well as the multi-measurement average. While most of these data sets have a common origin, they differ in how extensive temporal and spatial gaps in the coverage of ocean temperatures have been handled, ranging from data assimilation (Carton et al., 2018) to an iterative radius of influence mapping method (Cheng et al., 2017). The five data sets are all set to zero in 1986, which is the midpoint of the multi-measurement time series, by applying an offset for visual comparison. Since OHE, in units of W m^{-2}, is based upon the slope of each OHC data set, this offset has no impact on the computation of OHE from OHC that is central to our study. For the computation of OHE from OHC, we use a value of the surface area of the world's oceans equal to 3.3×10^{14} m^2 (Domingues et al., 2008). The OHC records we analyze are for the upper 700 m of the ocean. To calculate the OHE for the whole ocean, we multiply the OHE by 1/0.7 to account for the fact that the upper 700 m of the ocean holds 70% of the heat (Sect. 5.2.2.1 (Solomon, 2007)). When we subtract the amount of heat going into the ocean in Eq. 2 (Q_{OCEAN}), we also must account for the difference in surface area between the global atmosphere and the world's oceans. Since the Q_{OCEAN} term is computed for the surface area of the ocean, but the forcing is applied to the whole atmosphere, we multiply the

Q_{OCEAN} term by the ratio of the surface area of the ocean to the surface area of the atmosphere, which is 0.67.

As noted above, the calculation of χ^2_{OCEAN} shown in Eq. (8) is used to constrain our model representation of the temporal rise in OHC. Only model runs that provide a good fit to the observed OHC record are shown below. For these five OHC data sets, uncertainty estimates are not always provided. Furthermore, some studies that do provide uncertainties give estimates that seem unreasonably small (see Fig. S9 and the supplement). Because of the discrepancy in uncertainties between OHC records, we create a new uncertainty time series using both the 1-sigma standard deviation of the average of the five OHC records and the uncertainties from the Cheng 2017 OHC record. We create this new uncertainty from 1955-2019 by a monthly time step and use either the 1-sigma standard deviation of the average of the five OHC records or the uncertainties from the Cheng 2017 OHC record, whichever is larger, for that month. We use the Cheng 2017 OHC uncertainties because these estimates are the largest of the five data sets. Additionally, the standard deviation from the mean of the five OHC records is very low in the 1980s, which is an artifact of our normalization treatment, not inherent to any of the records. This combined uncertainty estimate is substituted in for each individual data set and the average, resulting in our use of the same time varying uncertainty in OHC for all data sets. Figure S9 and the supplement provide more detail on the creation of this time dependent uncertainty estimate for OHC.

The choice of OHC record has only a small effect on future projections of GMST using the EM-GC. Figure 4 illustrates the effect of varying OHC record on future temperature. The bottom panels show the observed and modeled OHC, the value of κ needed to best fit the OHC data record, as well as the resulting value of χ^2_{OCEAN}. Of the two OHC records shown, Balmaseda et al. (2013) (Fig. 4a) yields the lowest value of κ and Ishii et al. (2017) (Fig. 4b) results in the highest estimate of κ. For the same value of AER RF_{2011} (i.e., $-0.9\ \mathrm{W\ m^{-2}}$) and GHG scenario (SSP4-3.4), we find a difference of 0.25°C in the modeled rise in GMST in year 2100 for these two simulations (red lines on top panels). For most of the remaining analysis, we use the multi-measurement average of the five OHC data records. However, in Sects. 3.1 and 3.2 we quantify the effect of OHC data record on both attributable anthropogenic warming rate and equilibrium climate sensitivity.

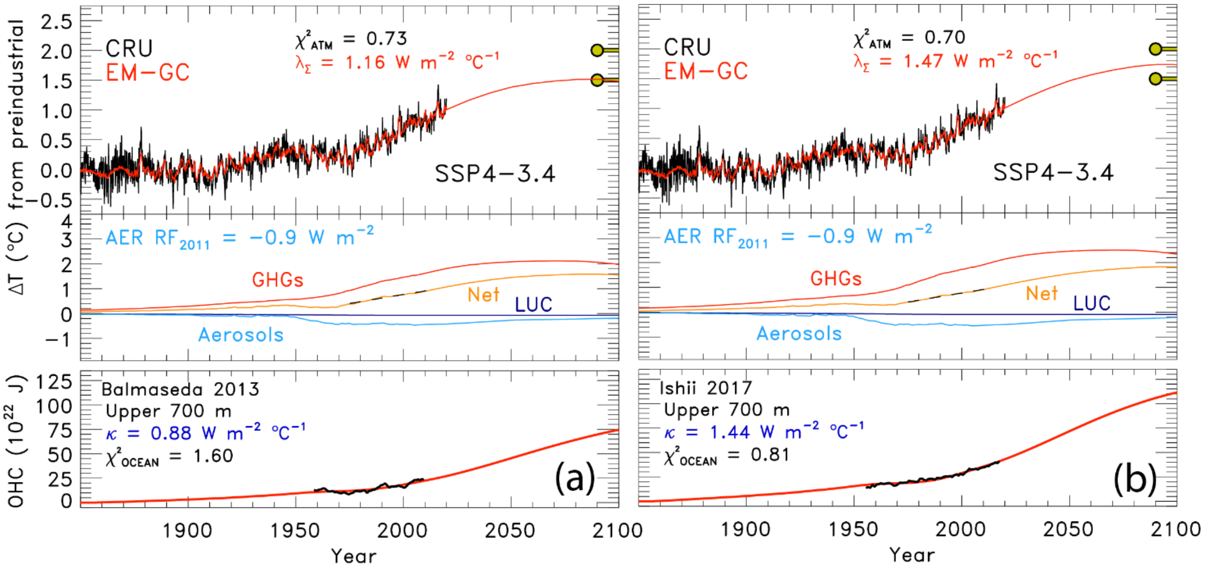

Figure 4. Measured and EM-GC simulated GMST change (ΔT) from 1850-2019, as well as projected ΔT to year 2100 for SSP4-3.4. Top panel of each plot shows observed (black) and simulated (red) ΔT, the λ_Σ and χ^2_{ATM} values, and the Paris Agreement target and upper limit. The second panel displays the contribution of GHGs, aerosols, and land use change on ΔT. The bottom panel compares the observed (black) and modeled (red) OHC for two different OHC records and displays the value of κ needed to provide best-fits to the OHC record, as well as best-fit values of χ^2_{OCEAN}. Both use an aerosol RF in 2011 of −0.9 W m^{-2}. (a) OHC record from Balmaseda et al. (2013). (b) OHC record from Ishii et al. (2017).

2.3 Attributable anthropogenic warming rate

The attributable anthropogenic warming rate, or AAWR, is the time rate of change of GMST due to humans from 1975-2014. We use AAWR as a metric in the EM-GC framework to quantify the human influence on global warming over the past few decades, and most importantly to also assess how well the CMIP6 GCMs can replicate this quantity. This analysis is motivated by the study of Foster and Rahmstorf (2011), who examined the human influence on the time rate of change of GMST from 1979-2010 using a residual method. We extend the end year of our analysis to 2014 because this is the last year of the CMIP6 Historical simulation. We pushed the start year back to 1975 so that our analysis covers a forty-year period, over which the effect of human activity on GMST rose nearly linear with respect to time (Fig. 1b and Fig. S10c).

We calculate AAWR utilizing the EM-GC by computing a linear fit to the $\Delta T_{HUMAN,ATM}$ term:

$$\Delta T_{ATM,HUMANi} = \frac{1+\gamma}{\lambda_p} \{GHG\ \Delta RF_i + AER\ \Delta RF_i + LUC\ \Delta RF_i - Q_{OCEAN}\} \qquad (9)$$

for a regression that spans 1850-2019. The $\Delta T_{HUMAN,ATM}$ term represents the net impact of the change in GMST due to RF of climate by anthropogenic GHGs, tropospheric aerosols, as well as the variation in surface reflectivity due to land use change (deforestation), taking into account that for each model time step, a portion of the human-induced climate forcing is exported to the world's oceans. For each simulation, the slope of the linear least squares fit to the 480 monthly values of $\Delta T_{HUMAN,ATM}$ is used to determine AAWR. For the time period 1975-2014, a value for AAWR of 0.144 ± 0.005 °C/decade is found using a value of AER RF_{2011} equal to -0.9 W m^{-2}, where the uncertainty corresponds to the 2-sigma standard error of a linear least squares fit. The computation of AAWR found by fitting monthly values of $\Delta T_{HUMAN,ATM}$ is insensitive to modest changes in start and end year for the AAWR calculation (see Table S1), as well as whether or not the AMOC, PDO, or IOD terms are included in the regression framework (Canty et al., 2013; Hope et al., 2017). We are able to fit the climate record better (i.e. smaller values of χ^2 in Eqs. (6), (7), and (8)) upon consideration of the AMOC term. However, computed values of AAWR are insensitive to whether this term is used in the regression because whatever contributions the variation in the strength of the thermohaline circulation may have had on GMST are not considered in Eq. (9) (see Sect. 2.3 of Hope et al. (2017) for further explanation).

The determination of AAWR from historical CMIP6 near surface air temperature output involves conducting a regression of deseasonalized, globally averaged, monthly ΔT ($\Delta T^{DES,GLB}$) from each GCM (Hope et al., 2017), termed the REG method. The archived CMIP6 Historical runs are constrained by observed variations in SAOD and influenced by other factors such as internal model generated ENSOs. The $\Delta T^{DES,GLB}$ time series for all of the runs from each CMIP6 GCM are averaged together to obtain one time series of $\Delta T^{DES,GLB}$ for each GCM. This average $\Delta T^{DES,GLB}$ time series is used to compute AAWR. The regression approach is used to compute the influence of SAOD on GMST from CMIP6 GCMs. The time needed for GMST to respond to a change in the aerosol loading in the stratosphere due to a volcanic eruption in each GCM can exhibit a significant difference compared to the empirically determined response time of 6 months discussed in Sect. 2.1. A lag was determined for each GCM by calculating the value of the monthly delay between volcanic eruptions and the surface temperature response that resulted in the largest regression coefficient for SAOD. We regress the $\Delta T^{DES,GLB}$ against SAOD and the anthropogenic effect on temperature, which is approximated as a linear function from 1975-2014. The value of AAWR is the slope of the anthropogenic effect on temperature. Figure S10 illustrates the REG method used to determine AAWR from the CMIP6 GCMs. Table S2 depicts the slight effect on values of AAWR for the CMIP6 GCMs of changing the start or end year for the regression. At the time of analysis, there are 50 CMIP6 GCMs with the necessary archived output to calculate AAWR, with the values of AAWR found using REG shown in Table S3.

We also use a second method to extract the value of AAWR from the CMIP6 multi-model ensemble. This method, termed LIN, involves the computation of a linear regression of global, annual average values of GMST from the CMIP6 multi-model ensemble (Hope et al., 2017). For LIN, we exclude the years of obvious volcanic influence on the rise in GMST from the CMIP6 multi-model ensemble Historical simulations: i.e. data for 1982 and 1983 (following the eruption of El Chichón) and 1991 and 1992 (following the eruption of Mount Pinatubo) are excluded. Archived global, annual average values of GMST covering 1975-2014, excluding these four years, are fit using linear regression, with the AAWR set equal to the slope of the fit. Values of AAWR for 1975-2014 found using LIN are also shown in Table S3 for each GCM. Analysis of AAWR for these 50 GCMs of LIN versus REG (see Fig. S11) results in a correlation coefficient (r^2) of 0.995 and a mean ratio of 1.009 ± 0.015, with LIN-based AAWR exceeding REG-based AAWR by about 1%. The close agreement of AAWR found using both methods provides strong evidence for the accurate determination of AAWR from the CMIP6 GCMs. We use the REG method in this analysis because it provides a more rigorous technique to remove the influence of SAOD on GMST from the CMIP6 multi-model ensemble compared to the LIN method. All of our scientific conclusions are unchanged had we used LIN-based values of AAWR from the CMIP6 multi-model ensemble.

2.4 Equilibrium climate sensitivity

The equilibrium climate sensitivity (ECS), which represents the warming that would occur after climate has equilibrated with atmospheric CO_2 at the 2×pre-industrial level (Kiehl, 2007; Otto et al., 2013;

Schwartz, 2012) is also used to compare results of our EM-GC to CMIP6 multi-model output. To calculate ECS from the EM-GC, we use the following equation:

$$ECS = \frac{1+\gamma}{\lambda_P} \times 5.35\ \mathrm{W\ m^{-2}} \times \ln(2) \qquad (10)$$

That represents the rise in GMST for a doubling of CO_2, assuming no other perturbations as well as equilibrium in other components of the climate system (i.e., $Q_{OCEAN} = 0$) (Mascioli et al., 2013). The expression for the radiative forcing of CO_2 is from Myhre (1998). The quantity γ in Eq. (10), which represents the sensitivity of the GMST to feedbacks within the climate system, is the only variable component of ECS. We only use values of γ that result in good fits ($\chi^2 \leq 2$ for Eq. (6) to (8)) between modeled and observed GMST and modeled and observed OHC.

For the estimate of ECS from the CMIP6 multi-model ensemble, we use the method described by Gregory et al. (2004). We use the Gregory method to calculate ECS from the CMIP6 GCMs because this procedure is preferred by Eyring et al. (2016) for the use by CMIP6. There have been some recent analyses that suggest the Gregory method may underestimate ECS (Rugenstein et al., 2020). However, we use the Gregory method to be consistent with the approach for CMIP6 recommended by Eyring et al. (2016).

To use the Gregory method, near surface air temperature output from the Abrupt 4×CO_2 and piControl simulations, as well as net downward radiative flux output from the Abrupt 4×CO_2 simulation is used to calculate ECS. At the time of this analysis, 28 models released the necessary output to the CMIP6 archive (see Table S4 for the list of models and individual values of ECS). The near surface air temperature and net downward radiative flux was converted from monthly gridded output to annual global averages. We calculate the temperature change for the Abrupt 4×CO_2 simulation by subtracting the piControl near surface air temperature (Chen et al., 2019) (Fig. S12). This computed temperature anomaly is then regressed against the net downward radiative flux, with the x-intercept yielding the equilibrium response of ΔT to a quadrupling of CO_2. This equilibrium response is then divided by two (Jones et al., 2019) to arrive at the equilibrium climate sensitivity (Fig. S12).

2.5 Aerosol weighting method

Probabilistic forecasts of the future rise in GMST for various SSPs are an important part of our analysis. Probabilities of AAWR and ECS are computed by considering the uncertainty in AER RF_{2011}. We also provide probabilistic estimates of AAWR and ECS. All of these quantities are computed by incorporating the uncertainty in the radiative forcing of climate due to tropospheric aerosols within results of our EM-GC simulations. We use an asymmetric Gaussian to assign weights to the value of GMST, AAWR or ECS found for various time series of radiative forcing by aerosols associated with particular values of AER RF_{2011}. Figure 5a shows the asymmetric Gaussian function we use to maximize the values of AAWR or ECS at the best estimate of AER RF_{2011} of −0.9 W m^{-2}, accomplished by giving these values the highest weighting. The IPCC 2013 "likely" range limits of AER RF_{2011} of −0.4 and −1.5 W m^{-2} (Myhre et al., 2013) are assigned to the one sigma values of the Gaussian, and the AAWR or ECS estimates occurring at the "likely" range AER RF_{2011} limits are given the same weighting. The −0.1 and −1.9 W m^{-2} limits of the AER RF_{2011} range are assigned as the two sigma values of the asymmetric Gaussian, based upon the IPCC 2013 description of these two values as being 5 and 95% uncertainty limits (Myhre et al., 2013). The Gaussian we use is asymmetric due to the fact that the distribution of the likely range and 5th and 95th percentiles of the values of AER RF_{2011} are not distributed symmetrically from the best estimate of −0.9 W m^{-2}. For example, the likely ranges of AER RF_{2011} are given as −0.4 W m^{-2} and −1.5 W m^{-2}; the −0.4 W m^{-2} value is 0.5 W m^{-2} from the best estimate whereas −1.5 W m^{-2} is 0.6 W m^{-2} from the best estimate.

We fit a Gaussian to the likely range and 5th and 95th percentiles that has slightly different shape on either side of the best estimate, as shown in Fig. 5a.

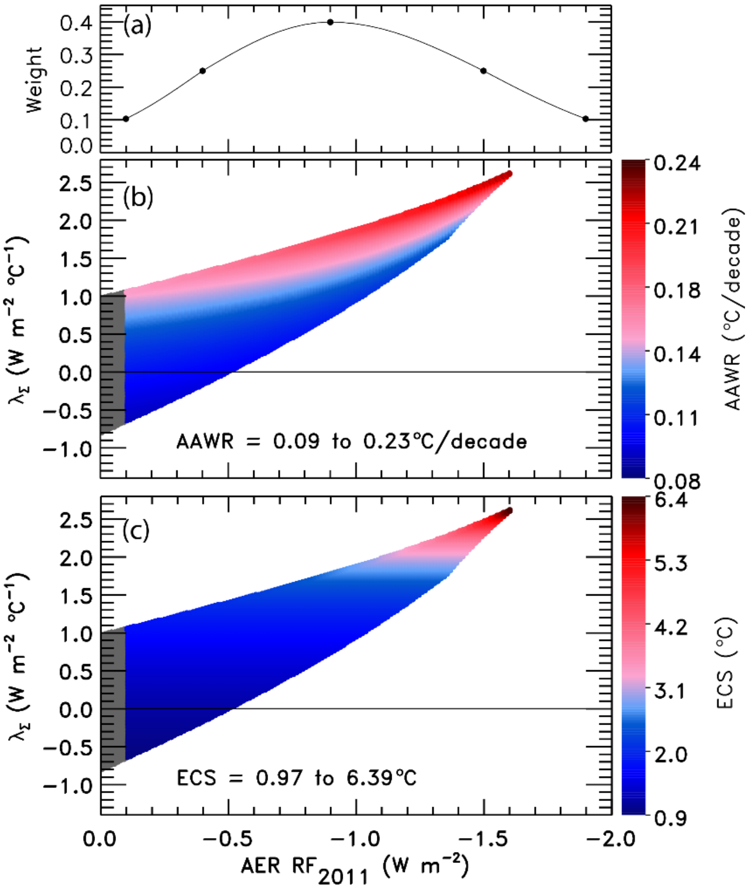

Figure 5. Aerosol weighting method. (a) The weights assigned to an asymmetric Gaussian distribution of AER RF$_{2011}$ based on values provided by chapter 8 of IPCC 2013. The five black circles indicate the assigned weights for the AER RF$_{2011}$ best estimate of −0.9 W m^{-2}, likely range of −0.4 and −1.5 W m^{-2}, and the 5th and 95th confidence intervals of −0.1 and −1.9 W m^{-2}. (b) Values of AAWR in °C/decade as a function of climate feedback parameter, λ_Σ, and the value of AER RF$_{2011}$ associated with various time series for the RF of climate due to tropospheric aerosols. The colors denote the various values of AAWR calculated from 1975-2014 using the EM-GC. (c) ECS in °C as a function of λ_Σ and the value of AER RF$_{2011}$. The colors denote various values of ECS found using the EM-GC. For panels (b) and (c), model results are shown only for combinations of λ_Σ and RF due to tropospheric aerosols for which good fits to the climate record could be achieved.

Figure 5b shows the value of AAWR in °C/decade as a function of the climate feedback parameter, λ_Σ, and AER RF$_{2011}$. We are able to find more good fits to the observed GMST for small values of AER RF$_{2011}$ than at larger values of AER RF$_{2011}$. Therefore, we bin values of AAWR (Fig. 5b), ECS (Fig. 5c), or future GMST (described in Sect. 3.3) by AER RF_{2011} and find the probability distribution for values of AAWR, ECS, or future GMST within each bin. The resulting probability distributions are assigned the weights associated with each value of AER RF_{2011} in the bins to arrive at the probabilistic estimates of AAWR or ECS shown in Sect. 3. If we did not use this procedure and instead simply averaged all of the values for AAWR and ECS shown in Fig. 5, undue emphasis would be given to model results that occur at small AER RF_{2011} (see Fig. S14 for unweighted ECS values). This aerosol weighting method allows the expert assessment of the likely range of RF due to tropospheric aerosols given in Chapter 8 of IPCC 2013 (Myhre et al., 2013) to be quantitatively incorporated into our computations of AAWR, ECS, and GMST.

3 Results

3.1 AAWR, comparison to CMIP6 multi-model ensemble

An important measure of any climate model is the ability to accurately simulate the human influence on the global mean surface temperature (GMST) anomaly. We use the attributable anthropogenic warming rate (AAWR) found by our highly constrained Empirical Model of Global Climate (EM-GC) to quantify how well the CMIP6 multi-model ensemble (see Table S5 for a list of CMIP6 GCMs analyzed in this study) is able to simulate the human influence on global warming over the past several decades. The EM-GC results in Fig. 6 have been constrained by blended near surface air temperature (TAS) and the temperature at the interface of the atmosphere and the upper boundary of the ocean (TOS) (Griffies et al., 2016). The CMIP6 multi-model output contains archived fields of TAS and TOS, whereas only a subset of GCM groups provide the archived land fraction needed to calculate blended near surface air temperature. Cowtan et al. (2015) compare the modeled and measured trend in global temperature over 1975-2014 and found a 4.0% difference in the trend upon the use of blended temperature from CMIP5 GCMs, rather than global modeled TAS. Their analysis focused on a comparison of modeled and measured temperature, not just the anthropogenic component. We have used the method of Cowtan et al. (2015) to create blended CMIP6 temperature output, for the CMIP6 GCMs that provide TAS, TOS, and the land fraction. Upon our use of blended CMIP6 temperature output for these GCMs, and calculation of AAWR for 1975-2014 as described in Sect. 2.3, we find that AAWR based upon blended CMIP6 temperature is 3.5% lower than AAWR found when using only TAS. Tokarska et al. (2020) estimate an effect of 0.013°C/decade in the trend of CMIP6 temperature output upon the use of blended CMIP6 temperature instead of TAS, while Cowtan et al. (2015) report a difference of 0.030°C/decade between the trend in observations and modeled output. Since the difference between values of AAWR found using blended CMIP6 temperature output and TAS is so small and does not affect any of our conclusions, we use TAS output from the CMIP6 multi-model archive because this choice allows the behavior of many more GCMs to be examined.

Figure 6 compares values of AAWR from 1975-2014 computed using our EM-GC with AAWR found utilizing archived output from the CMIP6 multi-model ensemble. Five GMST data sets and five OHC records can be used to estimate AAWR with the EM-GC; for each choice, AAWR exhibits sensitivity to the variation of the time series of radiative forcing due to tropospheric aerosols. Each box and whisker plot found using our EM-GC shows, for a particular choice of GMST and OHC data record, the 25th, 50th, and 75th percentiles of AAWR (box), and 5th and 95th percentiles (whiskers) found using the aerosol weighting method described in Sect. 2.5. The star symbol indicates the minimum and maximum values of AAWR for each value of GMST data set and OHC record. The choice of OHC record and GMST data set has a slight effect on AAWR, as shown by the colored EM-GC symbols in Fig. 6. For example, switching from using the HadCRUT record to the CW14 record increases the values of λ_Σ that result in good fits to the climate record, which in turn affects the values of AAWR. The estimate of the value of AAWR increases from 0.143°C/decade to 0.153°C/decade when using the Cheng OHC record and changing the GMST record from HadCRUT to CW14. The averages of the five 25th, 50th, and 75th percentiles of AAWR found using the HadCRUT data set for GMST are 0.115, 0.135, and

0.160°C/decade, respectively. The 5th and 95th percentile values of AAWR from HadCRUT are 0.097 and 0.195°C/decade.

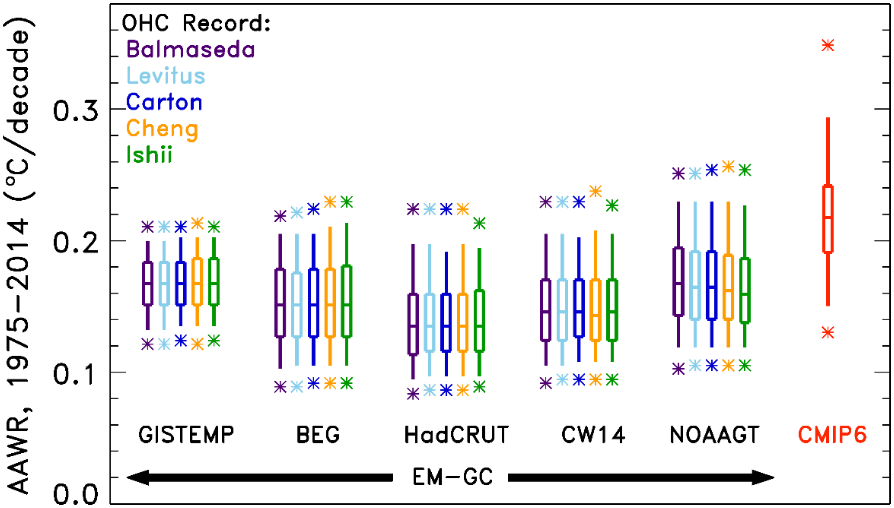

Figure 6. AAWR from the EM-GC and CMIP6 multi-model ensemble for 1975-2014. Five temperature data sets and five ocean heat content records are used to compare values of AAWR computed from the EM-GC. The box represents the 25th, 50th, and 75th percentiles, the whiskers denote the 5th and 95th percentiles, and the stars show the minimum and maximum values of AAWR from the EM-GC based upon the aerosol weighting method described in Sect. 2.5. The red box labeled "CMIP6" shows the 25th, 50th, and 75th percentiles, the whiskers represent the 5th and 95th percentiles, and the stars denote the minimum and maximum values of AAWR from the 50 member CMIP6 multi-model ensemble.

The box and whisker symbol labeled CMIP6 in Fig. 6 shows the 5th, 25th, 50th, 75th, and 95th percentiles of AAWR calculated from 50 GCMs, also from 1975-2014, as described in Sect. 2.3. The stars denote the minimum and maximum values of AAWR from the GCMs. Two CMIP6 models exhibit values of AAWR similar to the median values we infer from the HadCRUT, BEG, GISTEMP, NOAAGT, and CW14 data records using the EM-GC, in particular INM-CM5-0 (Volodin and Gritsun, 2018) yields 0.147°C/decade and MIROC6 (Tatebe et al., 2019) results in 0.157°C/decade (Table S3 provides values of AAWR for all individual CMIP6 GCMs). The median value of AAWR from the CMIP6 multi-model ensemble is 0.221°C/decade, about 60% larger than the 50th percentile value of AAWR found using the HadCRUT data set for GMST noted above. The 5th, 25th, 75th, and 95th percentiles of AAWR from the CMIP6 multi-model ensemble are 0.151, 0.192, 0.245, and 0.299°C/decade, respectively. Some CMIP6 GCMs exhibit values of AAWR that are almost 0.1°C/decade larger than our largest empirical estimates for 1975-2014; the maximum value of AAWR from the GCMs is 0.354 °C/decade. The maximum value of AAWR based off the historical climate record using the EM-GC is 0.257°C/decade (NOAAGT data set using the Cheng OHC record and a time series for RF due to tropospheric aerosols consistent with AER RF_{2011} equal to -1.6 W m^{-2}). The 95th percentiles of all EM-GC based values of AAWR in Fig. 6 are below the 75th percentile of AAWR from the CMIP6 multi-model ensemble of 0.245°C/decade, supporting the notion that CMIP6 GCMs tend to exhibit a faster rate of anthropogenic warming over the past four decades than the actual atmosphere.

Our determination that the rate of global warming from the CMIP6 multi-model ensemble over the time period 1975-2014 significantly exceeds the rise in GMST attributed to human activity is aligned with a similar finding highlighted in Figure 11.25b of chapter 11 of the IPCC 2013 report that CMIP5 models tend to warm too quickly compared to the actual climate system over the time period 1975-2014 (Kirtman et al., 2013). The values of AAWR from the CMIP6 multi-model ensemble from our analysis present a similar finding as Tokarska et al. (2020), that some of the CMIP6 models over estimate recent warming trends, with Tokarska et al. (2020) examining the trend in the human component of GMST from 1981-2014. We arrive at a similar conclusion that CMIP6 models overestimate the rate of global warming for the 1982-2014 time period of AAWR as shown in Table S2. Our results, the finding by the IPCC 2013 report, and Tokarska et al. (2020) appear to be quite different than the conclusion of Hausfather et al. (2020) that past climate models have matched recent temperature observations quite well. The Hausfather et al. (2020) study does not examine CMIP5 GCMs, let alone CMIP6 GCMs, and the last two rows of their Table 1 indicate that the skill of climate models forecasting the change in GMST over time decreased considerably between the Third Assessment Report (TAR) and the Fourth Assessment Report (AR4). The change in temperature over time for the TAR and AR4 only span 17 and 10 years, respectively (Hausfather et al., 2020). In Fig. 6, we examine the ability of the GCMs to simulate the rise in GMST attributed to humans over a 40 year time period, which provides a better measure of how well the models simulate the observations than when using a shorter time period. The temperature change over time for the TAR and AR4 examined by Hausfather et al. (2020) ends in 2017, which was right after a very strong ENSO, so their analysis may be influenced by the 2015 to 2016 ENSO event. In contrast, our analysis of AAWR is not influenced by natural variability such as ENSO because we examine the human component of global warming after explicitly accounting for and removing the influence of ENSO on GMST. Consequently, our determination of AAWR from observations (Table S1) and GCMs (Table S2) depends only to a small extent on the specification of start year (for values ranging from 1970 to 1984) and end year (2004 to 2018). Our analysis shows that upon quantification of the human driver to global warming within both the data record and climate models, the CMIP6 GCMs warm faster than observed GMST over the past four decades, regardless of precise specification of start and end year.

3.2 ECS

Equilibrium climate sensitivity (ECS) is a metric often used to compare the sensitivity of warming among GCMs, as well as with warming inferred from the historical climate record. Figure 7 shows values of ECS inferred from the climate record using our EM-GC, five GMST data sets, and five OHC records. As for AAWR, the largest variation in ECS is driven by uncertainty in AER RF_{2011}. The colored circles represent the ECS values found using the IPCC 2013 best estimate of AER RF_{2011} of −0.9 W m^{-2} (Myhre et al., 2013). The ECS values found utilizing the EM-GC are displayed using a box and whisker symbol. The middle line represents the median values of ECS, and the box is bounded by the 25th and 75th percentiles. The whiskers connect to the 5th and 95th percentiles, and the stars denote the minimum and maximum values. We use the aerosol weighting method described in Sect. 2.5 to calculate the percentiles for ECS; values of ECS found without aerosol weighting are shown in Fig. S14. Varying the choice of GMST data record has a slight effect on the value of ECS, whereas the choice of OHC record has a larger effect, as indicated by the various heights of the box and whiskers and the maximum values of ECS. In the EM-GC framework, the ocean heat export term (Q_{OCEAN}) represents disequilibrium in the climate system. We compute values of Q_{OCEAN} from various records of OHC. If the current value of Q_{OCEAN} is as large as suggested by the Cheng 2017 and Ishii et al. (2017) OHC records, then Earth's climate will exhibit a larger rise in GMST to reach equilibrium than if the value of Q_{OCEAN} inferred from the OHC record of Balmaseda et al. (2013) is correct. The averages of the 25th, 50th, and 75th percentiles of ECS found using the HadCRUT data set for GMST are 1.49, 1.85, and 2.50°C, respectively. The average best estimate of ECS using the HadCRUT data set and an AER RF_{2011} value of −0.9 W m^{-2} is 2.01°C.

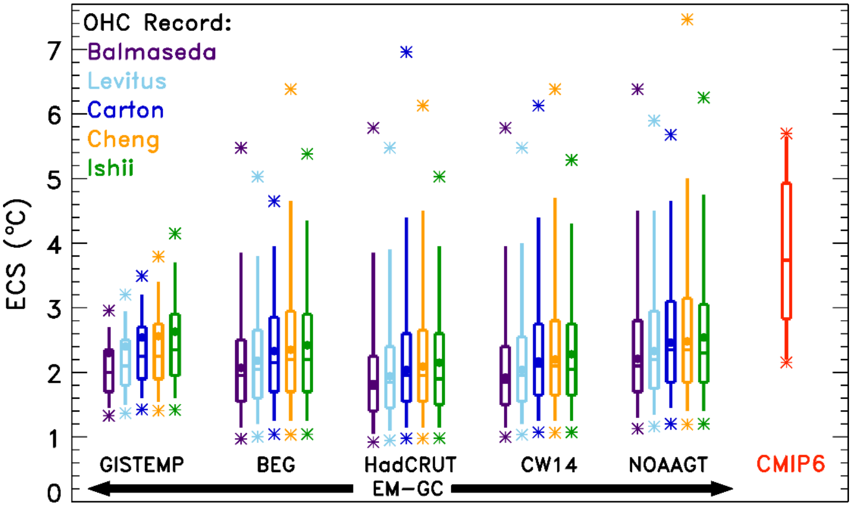

Figure 7. ECS from the EM-GC and the CMIP6 multi-model ensemble. Five GMST data sets and five ocean heat content records are used to compare values of ECS computed from the EM-GC. The box represents the 25th, 50th, and 75th percentiles, the whiskers denote the 5th and 95th percentiles, and the stars indicate the minimum and maximum values of ECS using the EM-GC based upon the weighting method described in Sect. 2.5. The circles denote the value of ECS associated with the best estimate of AER RF_{2011} of −0.9 W m^{-2}. The red box labeled "CMIP6" represents the 25th, 50th, and 75th percentiles, the whiskers denote the 5th and 95th percentiles, and the stars indicate the minimum and maximum values of ECS from the 28 member CMIP6 multi-model ensemble.

The box and whisker symbol labeled CMIP6 in Fig. 7 shows the 25th, 50th, 75th, and 5th and 95th percentiles of ECS calculated from output of 28 CMIP6 models, as described in Sect. 2.4. Minimum and maximum values are represented by the stars. The values of ECS from the CMIP6 multi-model ensemble are larger than the majority of values inferred from the climate record using the EM-GC. The height of the box for the CMIP6 multi-model ensemble estimate of ECS is larger than the height of the boxes for ECS inferred from the climate record using the EM-GC, indicating that the GCMs exhibit a wide range of ECS values. The 25th and 75th percentiles of ECS from the CMIP6 multi-model ensemble are 2.84°C and 4.93°C, respectively. The 5th percentile of ECS from the CMIP6 multi-model ensemble is 2.19°C, and the 95th percentile is 5.65°C (see Table S4 for ECS values for specific models). In contrast, the average 5th and 95th percentiles from the EM-GC are 1.12°C and 4.12°C, respectively. The median value of ECS from the CMIP6 multi-model ensemble is 3.74°C, more than double the median value of 1.85°C found using the HadCRUT temperature record.

We tested our approach of calculating ECS utilizing the EM-GC to CMIP6 GCMs by altering the EM-GC framework to include CMIP6 output (see the supplement for details). Our results in Fig. S13 show the validity of our approach. We obtain similar values of ECS for the CMIP6 GCMs using the EM-GC framework as the Gregory method. The EM-GC method is insensitive to which OHC record is used, as indicated in Fig. S13a and S13b.

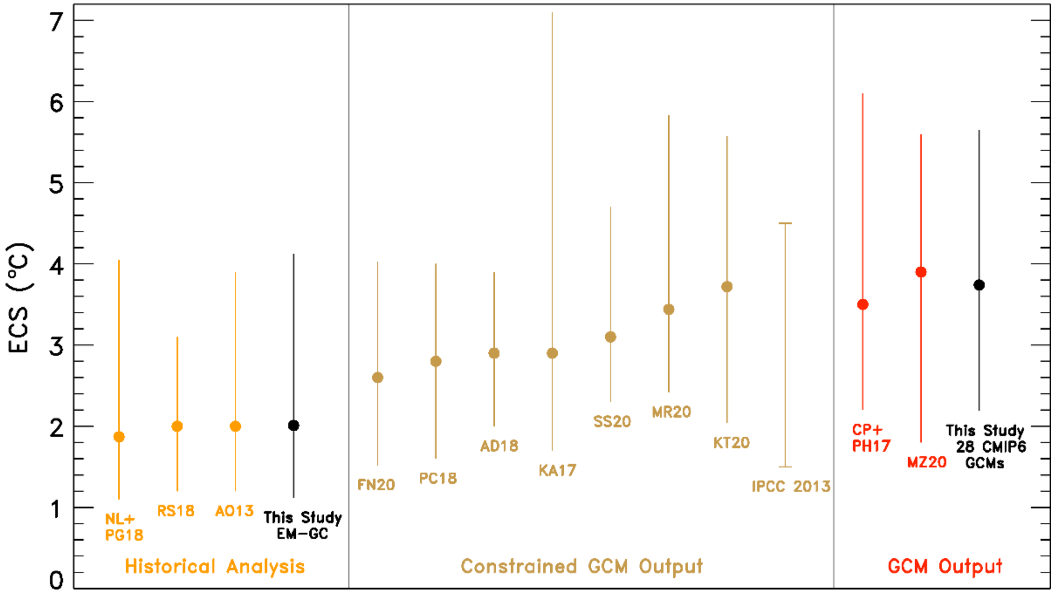

Figure 8. Values of ECS from the EM-GC (black), our analysis of the CMIP6 multi-model ensemble (black), and 13 other studies grouped by type of analysis. The studies are listed by lead author (first initial of their first name and first initial of their last name) and the year of publication, unless there are only two authors, in which case initials of both authors are listed. Historical analysis includes Lewis and Grünwald (2018) NL+PG18, Otto et al. (2013) AO13, and Skeie et al. (2018) RS18. Constrained GCM output includes Armour (2017) KA17, Cox et al. (2018) PC18, Dessler et al. (2018) AD18, Nijsse et al. (2020) FN20, Rugenstein et al. (2020) MR20, Sherwood et al. (2020) SS20, Stocker et al. (2013) IPCC 2013, and Tokarska et al. (2020) KT20. GCM output includes Proistosescu and Huybers (2017) CP+PH17 and Zelinka et al. (2020) MZ20.

Figure 8 summarizes values of ECS found utilizing the analysis of the century and a half long climate record using our EM-GC, our examination of a 28 member CMIP6 GCM ensemble, and 13 other recent studies. The studies are divided into three categories: those that estimated ECS based on observations (Historical Analysis), others that used GCM output but constrained the output in some way

(Constrained GCM Output), and studies that examined raw GCM output (GCM Output). We obtain a best estimate for ECS of 2.01°C using the HadCRUT data record and a value of AER $RF_{2011} = -0.9$ W m^{-2} with a range of ECS of 1.12-4.12°C (5th and 95th percent confidence interval). This estimate of ECS largely falls within the range provided by IPCC 2013 of 1.5°C to 4.5°C for ECS and is supported by three other derivations of ECS from the empirical climate record: 2.0°C (range of 1.2-3.9°C) given by Otto et al. (2013), 1.87°C (range of 1.1-4.05°C) given by Lewis and Grünwald (2018), and 2.0°C (range of 1.2-3.1°C) given by Skeie et al. (2018) (all range values are for the 5th and 95th percent confidence interval). Our estimate of ECS covers the same range of values given by Cox et al. (2018), Dessler et al. (2018), and Nijsse et al. (2020), as illustrated in Fig. 8. Our determination of ECS from the CMIP6 GCMs resembles that from Proistosescu and Huybers (2017) and Zelinka et al. (2020) as indicated in the GCM Output category of Fig. 8.

Recent studies have shown that the CMIP6 multi-model ensemble exhibits higher values of ECS than the CMIP5 models because of larger, positive cloud feedbacks within the latest models (Gettelman et al., 2019; Meehl et al., 2020; Sherwood et al., 2020; Zelinka et al., 2020). The IPCC 2013 report gives a likely range of 1.5°C to 4.5°C for ECS (Stocker et al., 2013), and some of the CMIP6 GCMs analyzed in this study have values of ECS more than 1°C above this range. However, some in the climate community seem to currently doubt whether the very large values of ECS are representative of the real world (Forster et al., 2020; Lewis and Curry, 2018; Tokarska et al., 2020). Gettelman et al. (2019) found that the newest version of the Community Earth System Model (CESM2) has a higher value of ECS than CESM1 (5.3°C versus 4.0°C) and urge the climate community to work together to determine the plausibility of such high values of ECS. Zhu et al. (2020) found that the high values of ECS in CESM2 and other GCMs is not supported by the paleoclimate record and are biased too warm. An analysis by Nijsse et al. (2020) obtains a median value of ECS from the CMIP6 multi-model ensemble of 2.6°C and range of 1.52-4.03°C (5th and 95th percentiles) coupled to a two-box energy balance model and the climate record. Similarly, Sherwood et al. (2020) conclude cooling during the Last Glacial Maximum provides strong evidence against ECS being greater than 4.5°C and conclude ECS lies within the range of 2.3 to 4.7°C at the 5th to 95th percent confidence intervals.

We obtain a wide range of ECS values from our EM-GC simulations of the climate record due to consideration of the uncertainty in the radiative forcing of climate due to tropospheric aerosols (Figs. 5c and 8). However, under one circumstance, we find values of ECS using the EM-GC that are similar to the maximum value of ECS from the CMIP6 multi-model ensemble. Our very large estimate of ECS occurs if we assume that anthropogenic aerosols have exhibited very strong cooling and offset a large amount of greenhouse gas warming, such that the observed GMST record can only be well simulated under the condition of large climate feedback (i.e., values of λ_Σ in Eq. (3) greater or equal to 2.5 W m^{-2} °C^{-1}). If aerosols have truly strongly cooled the climate, offsetting the vast majority of the rise in RF due to greenhouse gases as suggested by Shen et al. (2020), the actual value of ECS may lie close to 5°C or larger. Under the more likely scenario that aerosols have not cooled this strongly as suggested by Bond et al. (2013), then it is more feasible that ECS lies well below 5°C. The highest values of ECS found using our analysis (red portion of Fig 5c) are assigned low weights due to the assessment by Myhre et al. (2013) that the large AER RF_{2011} associated with these ECS values is unlikely.

Four empirical determinations of ECS (our study plus Lewis and Grünwald (2018), Otto et al. (2013), and Skeie et al. (2018)) and the CMIP6-constrained estimates of Cox et al. (2018), Dessler et al. (2018), and Nijsse et al. (2020) are in slight contrast with the 2.3-4.7°C range for ECS (5th and 95th confidence interval) published recently by Sherwood et al. (2020) (Fig 8). As noted above, Sherwood et al. (2020) use paleoclimate data to rule out the high range of ECS. They rely on a determination that the feedback due to clouds is moderately to strongly positive to rule out the low range of ECS found by our analysis and the studies noted above. We caution that knowledge of the cloud feedback from observations is generally limited to databases such as the International Satellite Cloud Climatology Project (ISCCP) (Schiffer and Rossow, 1983) and Pathfinder Atmospheres Extended (PATMOS-x) (Foster and Heidinger, 2013) that, while monumental in terms of complexity and scope, cover only a fairly short (i.e., about 36 years) part of the century and a half climate record (Klein et al., 2017; Sherwood et al., 2020). Most assessments of total cloud feedback rely on some combination of observations such as ISCCP, PATMOS-x, or other satellite records together with the results of regression analysis, GCM projections, and large eddy simulations that are able to resolve some of the convective processes involved in cloud formation (Klein et al., 2017; Sherwood et al., 2020). The most important component of the global cloud feedback is tropical low clouds, which Sherwood et al. (2020) consider to exert a positive feedback on climate based largely on the results of Klein et al. (2017). The determination by Klein et al. (2017) of a likely positive feedback for tropical low altitude clouds is based on the mean and standard deviation of the central value of this feedback determined by five studies, even though four of these studies exhibit uncertainties that encompass zero feedback and the fifth nearly reaches zero (their Fig. 3). This fact, combined with the recent study by Weaver et al. (2020) who report no long term statistically significant trend in global cloud reflectivity at 340 nm averaged between 45° S and 45° N based on analysis of data collected by a variety of NOAA and NASA satellite instruments, causes us to suggest the true value of ECS may lie below the 2.3°C lower limit given by Sherwood et al. (2020).

In our model framework, the largest uncertainty in ECS is driven by imprecise knowledge of the radiative forcing of climate by tropospheric aerosols. As shown in Fig. 5c, a wide range of ECS values can be inferred from the century and a half long climate record. We stress that each value of ECS shown in Fig. 5c is based upon a simulation for which χ^2_{ATM}, χ^2_{RECENT}, and χ^2_{OCEAN} are all less than or equal to 2. Better knowledge of AER RF for the contemporary atmosphere would lead to a reduction in the uncertainty of ECS. Numerous studies of the climate record, including our century and a half simulations, infer the possibility of lower values of ECS than was given by a recent analysis of studies that involve examination of data from compendiums such as ISCCP and PATMOS-x (Sherwood et al., 2020). However, Sherwood et al. (2020) did not examine consistency of the inferred value of ECS with the ability of models to accurately simulate the GMST anomaly between 1850 and present.

3.3 Future projections

3.3.1 CMIP6

The CMIP6 multi-model archive provides future projections of the GMST anomaly relative to pre-industrial (ΔT) using the ScenarioMIP Shared Socioeconomic Pathways (SSPs). Figure 9 shows the CMIP6 multi-model ensemble projections of ΔT for the four SSPs (SSP1-1.9, SSP1-2.6, SSP4-3.4, and SSP2-4.5) highlighted in our analysis. Each SSP scenario has varying amounts of gridded, monthly mean TAS projections submitted to the CMIP6 archive by GCMs (indicated on each plot). Global, monthly ΔT was created by averaging the TAS output over the globe with a cosine latitude weighting. The global, monthly ΔT time series for all of the runs for each CMIP6 GCM were averaged together to obtain one time series of ΔT. The varying amount of GCM output available for each SSP scenario is due to the fact that: a) SSP1-2.6 and SSP2-4.5 are Tier 1 scenarios (O'Neill et al., 2016) and are designated as priority over the other SSPs (as described in Sect. 2.2.2), and b) not all GCMs have provided results to the CMIP6 archive at the time of the analysis. More CMIP6 multi-model output will likely become available as modeling groups who have not submitted output to the CMIP6 archive finalize their results. However, we do not expect additional GCM simulations will affect our conclusions unless the GCM output is significantly different than that currently available.

The red trapezoid in Fig. 9 labeled as the IPCC 2013 likely range is the same trapezoid as that displayed on Figure 11.25b from chapter 11 of the IPCC 2013 report (Kirtman et al., 2013). All of the recent observations of ΔT from HadCRUT lie within the likely range of warming designated by this trapezoid. Many of the projections of the rise in ΔT from the CMIP6 multi-model ensemble lie above the IPCC 2013 likely range of warming. The Paris Agreement target of 1.5°C and upper limit of 2.0°C are shown as yellow circles, included to allow for comparison of the future projections of ΔT from the CMIP6 multi-model ensemble with the goals of the agreement. The thick blue line on each plot is the CMIP6 multi-model mean of ΔT, and the dashed blue lines are the minimum and maximum ΔT projections from the CMIP6 multi-model ensemble. For SSP1-1.9, the multi-model mean projection of ΔT in 2100 from the CMIP6 GCMs lies just above the Paris Agreement target at 1.6°C, whereas for SSP1-2.6 the CMIP6 multi-model mean reaches the Paris Agreement upper limit of 2.0°C at the end of this century. For both SSP4-3.4 and SSP2-4.5, the end of century CMIP6 multi-model mean lies above the Paris Agreement upper limit at 3.0°C and 3.1°C, respectively.

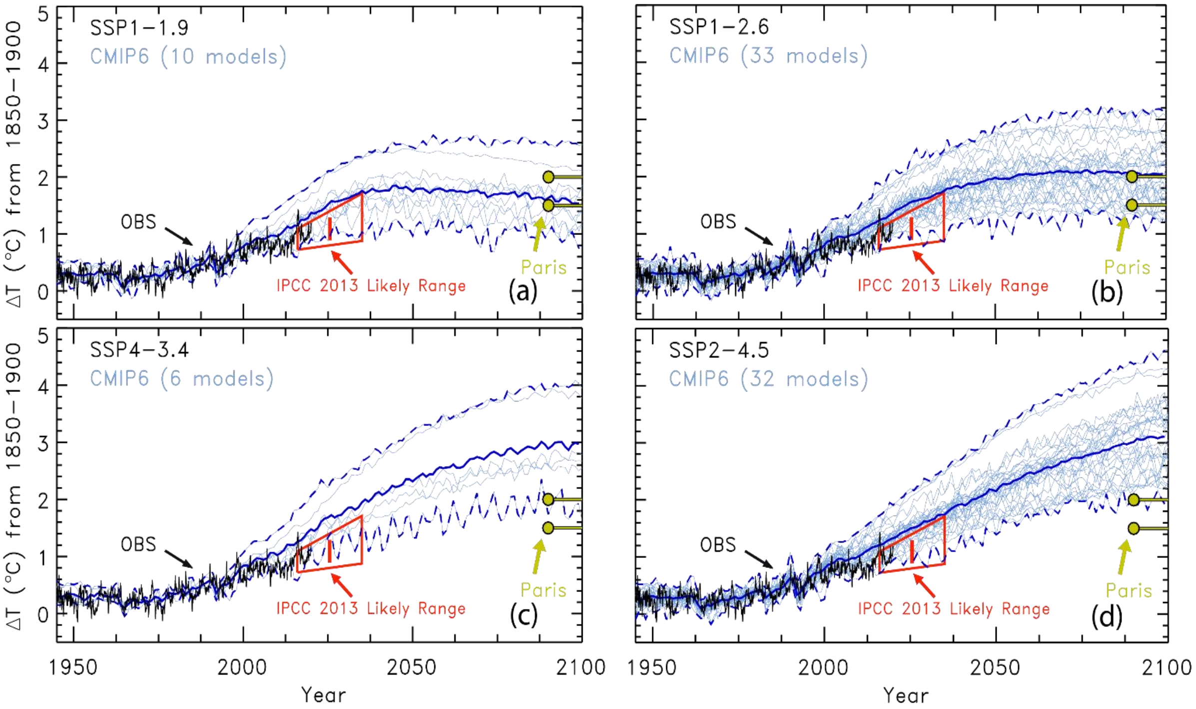

Figure 9. Historical simulations and future projections of GMST from the CMIP6 multi-model ensemble for several SSP scenarios. (a) GCM simulations from the Historical experiment, and future model projections from SSP1-1.9. Observations (black) are from HadCRUT to the end of 2019. The IPCC 2013 likely range of warming (red) is from Figure 11.25b from chapter 11 of the IPCC 2013 report. The CMIP6 multi-model mean (thick, blue) and minimum and maximum (dashed, blue) lines are shown. The Paris Agreement target of 1.5°C and upper limit (yellow) of 2.0°C are included to demonstrate how the GCM projections compare. (b) Future GMST projections from SSP1-2.6. (c) Future GMST projections from SSP4-3.4. (d) Future GMST projections from SSP2-4.5.

Figure 9 illustrates there is a bimodality of CMIP6 multi-model projections of ΔT, with a few GCMs having future values of ΔT that are considerably higher than others. This divergence for GCM projections of ΔT is especially evident in Fig. 9a, c, and d. The two CMIP6 GCMs that have the highest values of ΔT across the four SSPs are CanESM5 (Swart et al., 2019) and UKESM1 (Sellar et al., 2020). The CanESM5 and UKESM1 GCMs have the highest values of AAWR (0.354°C/decade and 0.299°C/decade, respectively), large values of ECS (5.70°C and 5.40°C, respectively), and exceed observed ΔT reported by HadCRUT for the past few decades (apparent in Fig. 9).

3.3.2 EM-GC

The EM-GC is also used to project future changes in ΔT using the SSPs. Figure 10 shows the GMST anomaly in 2100 from pre-industrial (ΔT_{2100}) as a function of the climate feedback parameter and AER RF_{2011}, for the four SSPs highlighted throughout. Only model runs from the EM-GC that achieved a good fit to the climate record ($\chi^2_{ATM} \leq 2$, $\chi^2_{RECENT} \leq 2$, $\chi^2_{OCEAN} \leq 2$) are shown. The EM-GC runs that satisfy these three χ^2 constraints but fall outside of the IPCC 2013 range for AER RF_{2011} (Myhre et al., 2013) are shaded grey (left hand side of each panel). We do not consider the EM-GC projections that lie outside of the IPCC 2013 range for AER RF_{2011} in our projections of ΔT, yet these results are shown to illustrate that the EM-GC can fit the climate record with estimates of the RF due to tropospheric aerosols that lie below (i.e., less cooling) of the 5th confidence interval of −0.1 W m^{-2} for AER RF_{2011} given by IPCC 2013. We cannot establish any good fits of the climate record for AER RF_{2011} with a cooling stronger

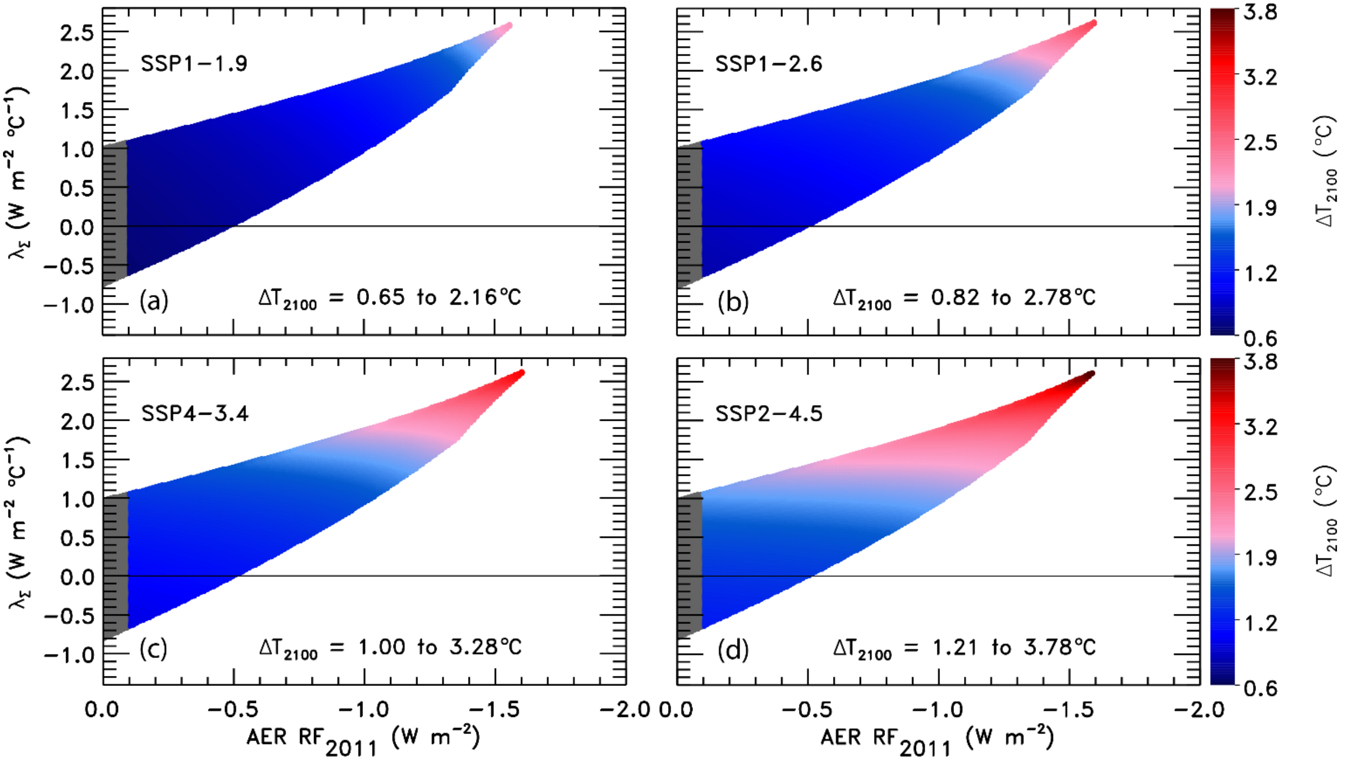

Figure 10. ΔT_{2100} as a function of climate feedback parameter and tropospheric aerosol radiative forcing in 2011 using the EM-GC. (a) Future GMST change for SSP1-1.9. The region outside of the AER RF_{2011} range provided by IPCC 2013 is shaded (grey). Colors denote the GMST change in year 2100 relative to pre-industrial. The color bar is the same across all four panels for comparison. (b) GMST anomaly for SSP1-2.6. (c) Future temperature change for SSP4-3.4. (d) GMST anomaly for SSP2-4.5.

than about −1.6 W m^{-2}. The range of ΔT_{2100} we compute using the EM-GC for SSP1-1.9, SSP1-2.6, SSP4-3.4, and SSP2-4.5 are 0.65-2.16°C, 0.82-2.78°C, 1.00-3.28°C, and 1.21-3.78°C, respectively. Results for SSP4-6.0, SSP3-7.0, and SSP5-8.5 are shown in Fig. S15: ΔT_{2100} ranges are 1.41-4.47°C, 1.84-5.56°C, and 2.13-6.75°C for these three scenarios.

The large range of ΔT_{2100} found for any given SSP scenario (i.e., a factor of 3.1 difference between the smallest and largest end of century warming for SSP2-4.5) is caused by the fact that the climate record can be fit nearly equally well by a considerably large combination of the climate feedback parameter (our λ_{Σ}) and scenarios for radiative forcing due to tropospheric aerosols. The more aerosols have cooled, offsetting the relatively well-known warming due to GHGs, the larger λ_{Σ} must be to fit the climate record. Since the RF of aerosols is set to diminish in the future due largely to public health concerns (Lelieveld et al., 2015; Shindell et al., 2016; Smith and Bond, 2014), the part of our model ensemble requiring relatively large values of λ_{Σ} to achieve a good fit to the climate record will result in higher values of ΔT_{2100} than other members of our model ensemble with small values of $\lambda_{\Sigma.}$ Most GCMs sample only a small portion of the possible combinations of λ_{Σ} and AER RF_{2011} shown in Figs. 10 and S8.

3.3.3 Comparing CMIP6 and EM-GC

Time series of future projections of ΔT from the EM-GC can be illustrated as probabilistic forecasts. Figure 11 shows the change in future ΔT for SSP1-1.9, SSP1-2.6, SSP4-3.4, and SSP2-4.5 colored by the probability of reaching at least that rise in ΔT by the end of the century. The EM-GC probabilities are computed from ensemble members for model runs constrained by the HadCRUT data records for GMST and the average of 5 OHC data records (Fig. S8) based upon the aerosol weighting method, described in Sect. 2.5. The trapezoid from chapter 11 of IPCC 2013 (Kirtman et al., 2013) is shown on Fig. 11 in black to highlight that the EM-GC projections of the future rise in ΔT lie within the IPCC 2013 likely range of warming. The Paris Agreement target and upper limit are included to compare the EM-GC projections of future ΔT to the Paris Agreement goals. The white shaded region is the EM-GC's median estimate of future ΔT for each SSP scenario. The median estimate for ΔT_{2100} for simulations using SSP1-1.9 and SSP1-2.6 falls below the Paris Agreement target at 1.0°C and 1.3°C, respectively.

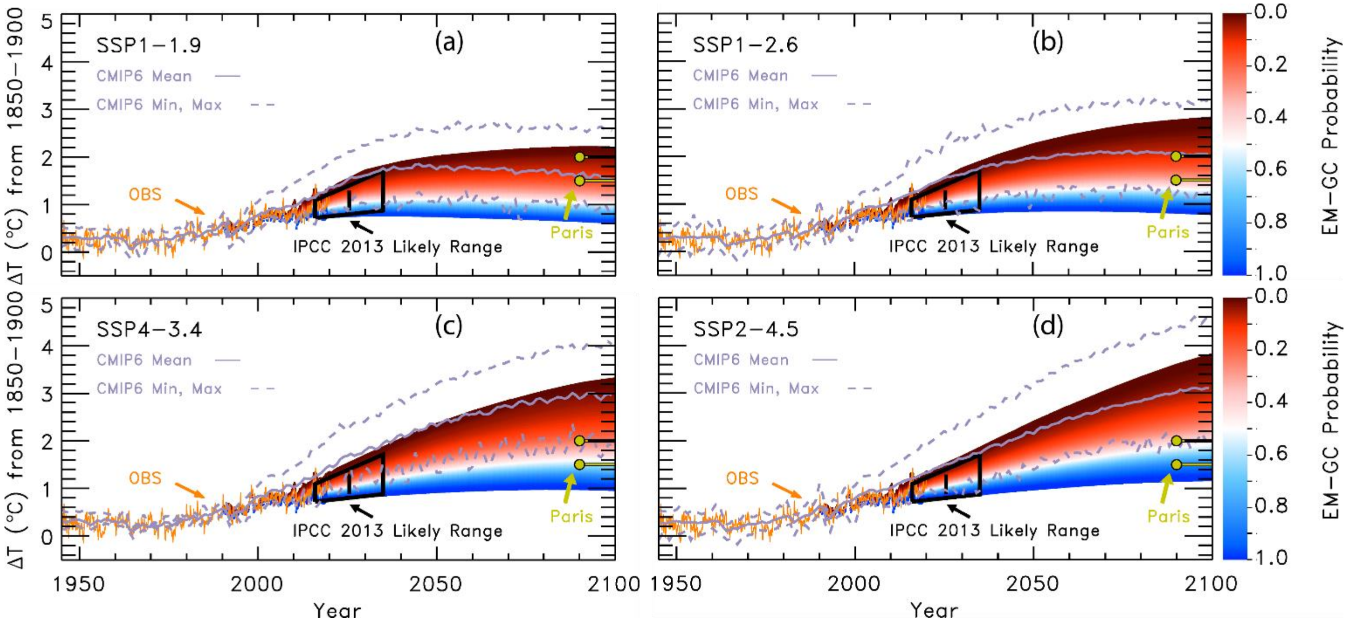

Figure 11. Probabilistic forecasts of the future rise in ΔT from the EM-GC for several SSPs. (a) Future projections of ΔT for SSP1-1.9. Observations (orange) are from HadCRUT. The IPCC 2013 likely range of warming (black) is from Figure 11.25b of chapter 11 of IPCC 2013. The Paris Agreement target and upper limit (yellow) are shown for comparison to EM-GC projections. The CMIP6 minimum, multi-model mean, and maximum values of ΔT are shown to compare to EM-GC projections. Colors denote the probability of reaching at least that temperature by the end of the century. (b) Future projections of ΔT for SSP1-2.6. (c) Future projections of ΔT for SSP4-3.4. (d) Future projections of ΔT for SSP2-4.5.

The median estimate of ΔT_{2100} from the EM-GC for SSP4-3.4 is between the Paris Agreement target and upper limit at 1.6°C. For SSP2-4.5 the median estimate of ΔT_{2100} is just below the Paris Agreement upper limit at 1.9°C. The CMIP6 minimum, multi-model mean, and maximum projections of ΔT, identical to those in Fig. 9, are also shown in Fig. 11. The CMIP6 minimum projection of the rise in ΔT falls near the EM-GC median estimate of ΔT for each SSP scenario. The CMIP6 multi-model mean value of the future change in ΔT falls below the EM-GC maximum value of ΔT, while the CMIP6 maximum value is far above the maximum projections of the future rise in ΔT using the EM-GC. Results for SSP4-6.0, SSP3-7.0, and SSP5-8.5 are provided in Fig. S16.Figure 12 compares probability distribution functions (PDFs) for the projection of ΔT_{2100} utilizing the EM-GC with the HadCRUT GMST record and average of the five OHC data set and the CW14 GMST record combined with the Cheng 2017 OHC record, and the CMIP6 multi-model ensemble. The CW14 PDF is shown to illustrate the slight sensitivity of our projections of ΔT_{2100} to the choice of GMST and OHC records. For the CMIP6 multi-model results, we compute the probabilities of achieving the Paris Agreement target of 1.5°C and upper limit of 2.0°C (at the end of the century) by calculating how many of the GCMs participating in each scenario have projections of ΔT_{2100} below the target or upper limit. In contrast, the probabilities for the projections of ΔT_{2100} using our EM-GC are computed using the aerosol weighting method, described in Sect. 2.5. The height of each histogram represents the probability that a particular range of ΔT_{2100}, defined by the width of each line segment, will occur. The left-hand y-axis displays the probability of ΔT_{2100} using the EM-GC, while the right-hand y-axis represents the probability of ΔT_{2100} using the CMIP6 multi-model simulations. The values on the CMIP6 multi-model ensemble y-axis are double the values on the EM-GC y-axis, for visual comparison. The solid black line denotes the Paris Agreement target and the dotted

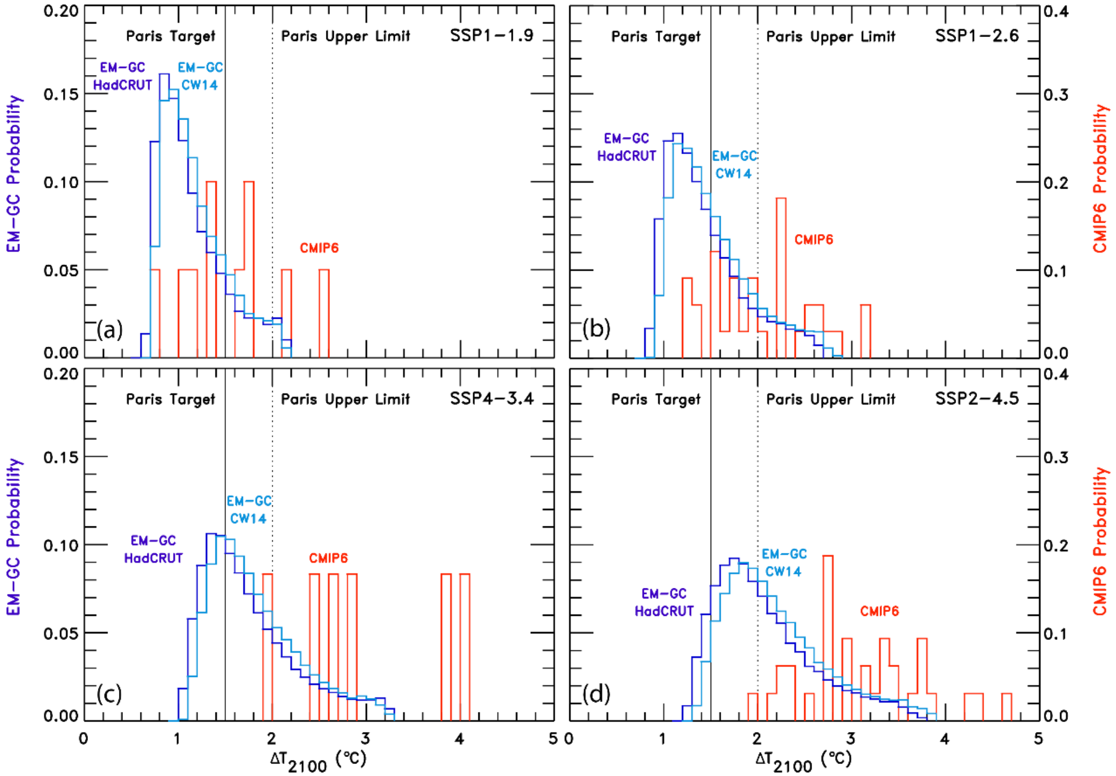

Figure 12. Probability density functions (PDF) for ΔT_{2100} found using the EM-GC with the HadCRUT temperature record (dark blue), the EM-GC with the CW14 temperature record (light blue), and CMIP6 multi-model results (red). (a) PDF for EM-GC results and CMIP6 multi-model results for SSP1-1.9. The left-hand y-axis is for EM-GC probabilities and the righthand y-axis is for the CMIP6 multi-model ensemble probabilities. (b) PDF for SSP1-2.6. (c) PDF for SSP4-3.4. (d) PDF for SSP2-4.5.

black line signifies the upper limit on each panel. The PDFs for SSP4-6.0, SSP3-7.0, and SSP5-8.5 are shown in Fig. S17.

Numerical values of probabilities for staying at or below the Paris Agreement target or upper limit for all seven SSP scenarios are given in Table 1. Results utilizing the EM-GC and HadCRUT GMST combined with the average OHC are shown in the top half of the table, and probabilities using the CW14 GMST and Cheng 2017 OHC records are shown in the bottom half. The CMIP6 multi-model projections exhibit lower probabilities of achieving the goals of the Paris Agreement than the projections using the EM-GC. In the creation of ScenarioMIP, SSP1-2.6 was designed to be a scenario that achieved the Paris Agreement goals and likely (greater than 66% probability (Stocker et al., 2013)) limited warming below 2.0°C, and was expected to produce a future rise in ΔT_{2100} of 1.7°C (O'Neill et al., 2016). The CMIP6 multi-model probability of SSP1-2.6 to stay at or below 2.0°C is 51.5%, as shown in Table 1. Based on our analysis, the CMIP6 multi-model ensemble does not indicate SSP1-2.6 as being a 2.0°C pathway, because it will only provide about a 50:50 likelihood of limiting warming below 2.0°C.

Table 1. .List of SSP scenarios analyzed in this study and the probabilities of achieving the Paris Agreement target or upper limit based on the EM-GC using the HadCRUT4 GMST data set and average of the five OHC records and the CMIP6 multi-model ensemble. The second half of the table shows the probabilities of achieving the Paris Agreement target or upper limit based on the EM-GC using the CW14 GMST record and Cheng 2017 OHC data set. The probabilities using the EM-GC are computed using the aerosol weighting method. The probabilities using the CMIP6 models are computed by calculating how many of the models for that scenario are below the temperature limits compared to the total number of models.

	Probability of Staying at or Below 1.5°C		**Probability of Staying at or Below 2.0°C**	
	EM-GC	**CMIP6**	**EM-GC**	**CMIP6**
SSP1-1.9	84.1%	50.0%	96.7%	80.0%
SSP1-2.6	64.8%	15.2%	88.4%	51.5%
SSP4-3.4	37.6%	0.0%	74.0%	16.7%
SSP2-4.5	10.5%	0.0%	53.1%	3.1%
SSP4-6.0	0.6%	0.0%	26.6%	0.0%
SSP3-7.0	0.0%	0.0%	1.3%	0.0%
SSP5-8.5	0.0%	0.0%	0.0%	0.0%

	Using CW14 and Cheng OHC Record	
SSP1-1.9	82.4%	97.5%
SSP1-2.6	57.0%	85.5%
SSP4-3.4	28.1%	69.6%
SSP2-4.5	4.2%	43.2%
SSP4-6.0	0.0%	17.4%
SSP3-7.0	0.0%	0.0%
SSP5-8.5	0.0%	0.0%

Projections of ΔT_{2100} based on the EM-GC provide more optimism for achieving the Paris Agreement goals than the CMIP6 multi-model ensemble. The SSP1-1.9 scenario results in an 84.1% probability of ΔT_{2100} staying at or below 1.5°C, while SSP1-2.6 gives a 64.8% likelihood of global warming staying at or below 1.5°C by end of century (Table 1) using the HadCRUT temperature record. The probabilities decrease to 82.4% and 57.0% upon the use of the CW14 temperature record and OHC from Cheng 2017. The SSP1-1.9 scenario involves extreme climate mitigation that is unlikely to happen in the next few years with atmospheric CO_2 peaking close to present day values (Fig. 2a). The SSP1-2.6 scenario requires less climate mitigation than SSP1-1.9 (though still requires net negative emissions towards the end of the century) and provides greater than a 50% likelihood of staying at or below the Paris Agreement target, thus we designate SSP1-2.6 as the 1.5°C pathway in our model framework instead of SSP1-1.9. This result is supported by Tokarska et al. (2020), who show that the SSP1-2.6 scenario has a likely range of warming at 1.33-1.99°C above preindustrial by end of century, based upon filtering CMIP6 GCM output on the level of agreement with the observed climate record. Previous studies suggested that a 2.6 W m^{-2} scenario was in line with the 2.0°C goal (Kriegler et al., 2014, 2015; O'Neill et al., 2016; Riahi et al., 2015). However, our analysis suggests the 2.6 W m^{-2} scenario provides between a 57-65% probability of achieving the more stringent 1.5°C target depending on the choice of GMST and OHC data records, and that a 3.4 W m^{-2} scenario (i.e., SSP4-3.4) is in line with the 2.0°C goal and has about a 70-74% probability of limiting warming to 2.0°C (Table 1) depending on the choice of the same data records. We therefore designate SSP4-3.4 as the 2.0°C pathway. Significant climate mitigation efforts will be required to keep the growth of CO_2, CH_4, and N_2O below the trajectories shown for SSP1-2.6 (1.5°C pathway in our model framework) and SSP4-3.4 (2.0°C pathway) (Fig. 2).

3.3.4 Transient climate response and carbon budgets

The transient climate response to cumulative emissions (TCRE) relates the rise in ΔT to the cumulative amount of carbon released to the atmosphere by human activities. We illustrate TCRE from the EM-GC as probabilistic forecasts, as shown in Fig. 13, to analyze future projections of ΔT. Figure 13 displays the GMST anomaly from pre-industrial versus the cumulative emissions of CO_2, in Gt C, since 1870. The orange line represents observations of ΔT from HadCRUT plotted against cumulative carbon emissions from the Global Carbon Budget project (Friedlingstein et al., 2019). The colors represent the probability that ΔT will rise to the indicated level, considering only acceptable fits to the climate record, for the EM-GC ensemble run constrained to match GMST from HadCRUT and the mean OHC record from the five OHC data records (Fig. S8) and using the aerosol weighting method. The dotted and dashed horizontal lines are placed at ΔT values of 1.5°C and 2.0°C, the target and upper limit of the Paris Agreement. The intersections of the light grey curve with the dotted horizontal line represent the 95% probability of the Paris Agreement target being achieved, and the intersections of the light grey curve with the dashed horizontal line represent the 95% probability of the Paris Agreement upper limit being achieved. The intersection of these horizontal lines with the dark grey and the black curves are the 66% and 50% probabilities, respectively of the Paris Agreement target or upper limit being attained. The SSP5-8.5

scenario was used to calculate TCRE because this scenario has the highest cumulative carbon emissions needed to provide the most complete relation between ΔT and future emissions.

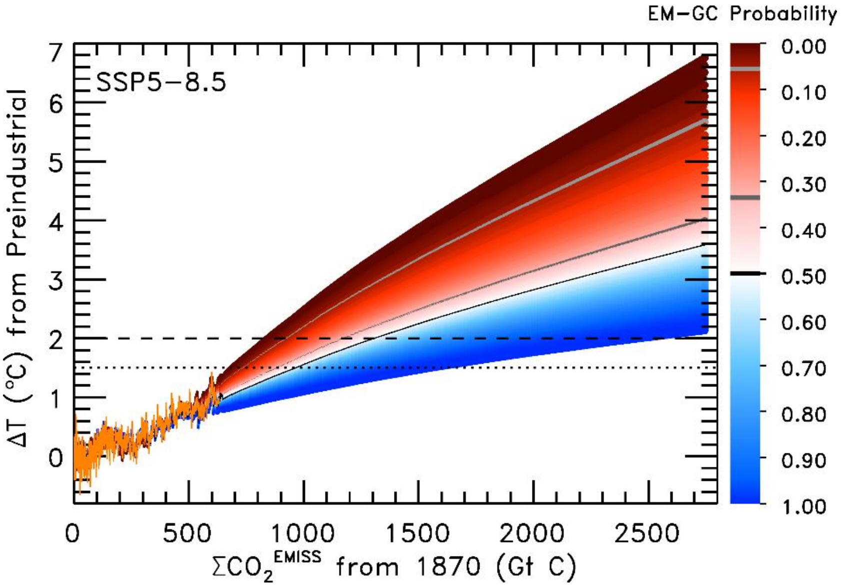

Figure 13. Transient climate response to cumulative CO_2 emissions for SSP5-8.5 using the EM-GC. Simulations of the rise in ΔT versus cumulative CO_2 emissions in units of Gt C. The orange line is observations of ΔT from HadCRUT plotted against cumulative carbon emissions from the Global Carbon Budget project (Friedlingstein et al., 2019). The dotted and dashed lines denote the Paris Agreement target and upper limit, respectively. The EM-GC projections represent the probability that the future value of ΔT will rise to the indicated level, considering only acceptable fits to the climate record. The light grey, dark grey, and black curves denote the 95, 66, and 50% probabilities of either the Paris target (intersection of dotted horizontal lines) or upper limit (intersection of dashed lines with curves) being achieved.

Table 2 contains estimated carbon budgets from our analysis in the form of the total CO_2 emissions (Gt C) since 1870 that result in a 95%, 66%, and 50% probability of the future rise in ΔT staying below the Paris Agreement target and upper limit and the future CO_2 emissions since 2019. Examination of Friedlingstein et al. (2014) and Murphy et al. (2014) led to our determination that the uncertainty in estimates of atmospheric CO_2 from emissions driven runs of CMIP5 coupled atmospheric / carbon cycle models is about 10% (1-sigma). We therefore use 10% as the uncertainty in how atmospheric CO_2 will respond to the prescribed carbon emissions. We apply the 10% uncertainty estimate to the future remaining carbon budget. To obtain a 95% likelihood of limiting the rise in future ΔT below 1.5°C, only 746 ± 75 Gt C since 1870 can be released into the atmosphere. For a 66% likelihood, 906 ± 91 Gt C can be released, while for a 50% probability 974 ± 97 Gt C in total can be emitted. To have a 95% probability of ΔT staying below the 2.0°C upper limit, 933 ± 93 Gt C since 1870 can be released into the atmosphere. For a 66% likelihood of the rise in ΔT staying below the upper limit, 1,203 ± 120 Gt C can be emitted, whereas for a 50% likelihood 1,323 ± 132 Gt C can be released. To place these numbers in their proper perspective, about 638 Gt C have been released from 1870 through the end of 2019 due to land use change, fossil fuel emissions, gas flaring, and cement production according to the Global Carbon Budget project (Friedlingstein et al., 2019). In our model framework, after 2019 society can therefore only emit another 108 ± 75, 268 ± 91, or 336 ± 97 Gt C to have either a 95%, 66%, or 50% chance of limiting warming to 1.5°C. These future emissions estimates rise to 295 ± 93, 565 ± 120, and 685 ± 132 Gt C to have a 95%, 66%, or 50% chance of limiting warming to 2.0°C.

Table 2. Total cumulative and future carbon emissions that will lead to crossing the Paris temperature thresholds based on the EM-GC. Estimates of $\Sigma CO_2^{EMISSIONS}$ that would cause global warming to stay below indicated thresholds for 95%, 66%, and 50% probabilities. The values in the top half of the table are the estimates of total cumulative carbon emissions that will lead to crossing the Paris Agreement thresholds with the 10% uncertainty included. The values in the bottom half of the table are the estimates of future cumulative carbon emissions after 2019 that will lead to crossing the Paris Agreement thresholds, with the same 10% uncertainty. The range of years given represents when the Paris Agreement thresholds will be passed based upon the rate of emissions from SSP5-8.5 or continuing the 2019 rate of emissions of 11.7 Gt C yr^{-1}.

Total $\Sigma CO_2^{EMISSIONS}$ since 1870 from the EM-GC			
	95%	**66%**	**50%**
1.5°C	746 ± 75 Gt C	906 ± 91 Gt C	974 ± 97 Gt C
2.0°C	933 ± 93 Gt C	1203 ± 120 Gt C	1323 ± 132 Gt C
Future $\Sigma CO_2^{EMISSIONS}$ (assuming 638 Gt C released between 1870-2019)			
	95%	**66%**	**50%**
1.5°C	108 ± 75 Gt C (2022[a]-2032[a]) (2021[b]-2034[b])	268 ± 91 Gt C (2032-2042) (2034-2049)	336 ± 97 Gt C (2036-2045) (2039-2056)
2.0°C	295 ± 93 Gt C (2033[a]-2043[a]) (2036[b]-2052[b])	565 ± 120 Gt C (2046-2056) (2057-2077)	685 ± 132 Gt C (2051-2061) (2066-2088)

[a] Year the 1.5°C target or 2.0°C upper limit will be exceeded assuming the rate of emission inferred from SSP5-8.5 and the 1-sigma uncertainty

[b] Year the 1.5°C target or 2.0°C upper limit will be exceeded assuming the 2019 rate of emission of 11.7 Gt C yr^{-1} and the 1-sigma uncertainty

An analysis by van Vuuren et al. (2020) assesses TCRE based on cumulative emissions after 2010. Their analysis indicates only 228 Gt C can be released since 2010 to have a 66% probability of achieving the Paris Agreement target of limiting the rise in ΔT below 1.5°C in 2100. They base this estimate on an analysis of climate sensitivity and carbon cycle components, including an adjustment to TCRE for the tendency of CMIP5 GCMs to warm too quickly that had been suggested by Millar et al. (2017). In our model framework, we find a 66% probability of limiting warming to 1.5°C upon the release of 369 ± 91 Gt C between 2010 and 2100. It is not surprising our analysis provides somewhat more latitude for the probabilistic forecasts of limiting warming to 1.5°C compared to estimates based on analyses of GCM output, given the tendency of CMIP5 GCMs (Hope et al., 2017) and CMIP6 GCMs (Sect. 3.1) to warm so much faster than the observed climate system. Regardless, between 2010 and 2019, about 101 Gt C has been released to the atmosphere (Friedlingstein et al., 2019), so the remaining budget after 2019 for limiting warming to 1.5°C is about 127 Gt C according to van Vuuren et al. (2020). At the pace of emissions in 2019 of 11.7 Gt C yr^{-1}, society will cross this threshold in about a decade. Our model framework suggests a remaining budget of 268 ± 91 Gt C (Table 2). Society has at most about 20 years, or 15-29 years based on the 10% uncertainty, to severely limit carbon emissions to have a 66% probability to achieve the target of the Paris Agreement.

3.3.5 Blended methane

Atmospheric abundances of methane will likely continue to increase as society expands natural gas production and agriculture, making it important to analyze the impact of various methane scenarios on the rise of GMST. It is unlikely future atmospheric methane abundances will progress as indicated by SSP1-2.6 (see Fig. 2), a low radiative forcing scenario. Current observations shown in Fig. 2 illustrate that the methane mixing ratio is following SSP2-4.5 and has missed the initial decline needed to follow the SSP1-2.6 pathway. To analyze the effect varying future methane abundance pathways will have on GMST, we have generated linear interpolations of the SSP1-2.6 and SSP3-7.0 methane future abundances and created four alternate scenarios (see Fig. S18), which we call blended methane scenarios. We can substitute one of the blended methane scenarios into the EM-GC instead of using the projection of methane specified by the SSP database to quantify the sensitivity of future warming to various evolutions of methane on the rise in GMST.

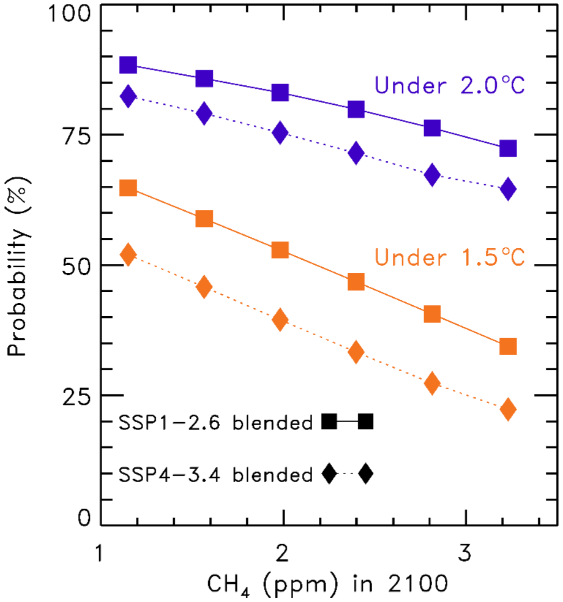

Figure 14. Probability of staying at or below the Paris Agreement target and upper limit for SSP1-2.6 and SSP4-3.4 as a function of varying methane scenarios using the EM-GC. The atmospheric methane scenarios are calculated using linear combinations of methane abundances from SSP1-2.6 and SSP3-7.0 to span the range of future methane abundances.

Figure 14 shows the probability of staying at or below the Paris Agreement target (gold colors) or upper limit (purple colors) for SSP1-2.6 (solid) and SSP4-3.4 (dotted) as a function of the methane mixing ratio in 2100. The lowest atmospheric methane mixing ratio value in 2100 of 1.15 ppm is from the SSP1-2.6 methane pathway, the highest mixing ratio in 2100 of 3.20 ppm is from the SSP3-7.0 methane pathway, and the four in between are the blended methane scenarios. As the atmospheric methane abundance increases, the likelihood of achieving the goals in the Paris Agreement decreases. For SSP1-2.6, the probability of limiting the rise in GMST below the 1.5°C target begins at 65% using the SSP1-2.6 designated methane pathway and decreases as the blended scenarios are considered. The probability of achieving the Paris Agreement target declines to just under 50% if methane reaches 2.4 ppm in 2100 and to 34% if methane increases to 3.2 ppm in 2100. Even though we have labeled SSP1-2.6 the 1.5°C pathway in our model framework, limiting future warming to this challenging amount can likely only be achieved by strict limits on both emissions of carbon dioxide and methane.

In Sect. 3.3.3, we showed that if all GHGs follow the SSP4-3.4 scenario there would be a 74% probability of limiting warming to 2.0°C. If the methane pathway instead follows SSP1-2.6, which has an end of century mixing ratio of only 1.15 ppm, then the probability of achieving the Paris Agreement goal rises to 82%. However, if the methane pathway follows SSP3-7.0 and the end of century mixing ratio increases to 3.2 ppm, then the probability of achieving the Paris Agreement goal declines to 65%.

Reducing the future anthropogenic emissions of methane might be more challenging than controlling future emissions of carbon dioxide, simply because methane has such a wide variety of sources related to energy, agriculture, and ruminants (Kirschke et al., 2013). Given the current widespread use of methane as a source of energy in the United States and parts of Europe (Saunois et al., 2020), combined with the continued growth in the global number of ruminants (Wolf et al., 2017), it seems unrealistic for atmospheric methane to follow the peak and sharp decline starting in 2025 of the SSP1-2.6 pathway (Fig. 3b). Our analysis suggests failure to limit methane to the SSP1-2.6 trajectory will have a larger impact on the achievement of the 1.5°C Paris goal compared to the 2.0°C upper limit. Figure 14 is designed to provide some perspective on the importance of future controls on limiting the growth of methane on projections of end of century warming.

3.3.6 Climate feedback

In our analysis above, we have assumed the value of λ_Σ (and thus λ, see Eq (3) and corresponding text in Sect. 2.1) is constant over time. Time-constant λ_Σ is the simplest assumption one can make. The climate record can be fit very well based on this conjecture, as shown in Fig. 1a and Fig. S3a. However, many GCMs suggest that climate feedback may vary over time (Marvel et al., 2018; Rugenstein et al., 2020). In our EM-GC framework, we are able to conduct calculations allowing the value of λ_Σ to vary over time, and to project future temperature with such an assumption. Up until this point, our simulations have used λ_Σ to be consistent with how our model results had been presented in prior publications (Canty et al., 2013; Hope et al., 2017). Recall from Sect. 2.1 that $\lambda_\Sigma = \lambda_P - \lambda$. To assess the effect of time varying climate feedback on our projections of global warming, we examine the sensitivity in terms of λ^{-1}, because this quantity scales proportionally with ΔT and also our use of the inverse λ allows for direct comparison to the results of Marvel et al. (2018) and Rugenstein et al. (2020).

Figure 15 shows the change in observed and modeled GMST under several assumptions regarding λ^{-1}. The first assumption is that the value of λ^{-1} is constant over time (Figs. 15a, e). We are able to fit the climate record over the past 170 years (χ^2_{ATM}) and past 80 years (χ^2_{RECENT}) extremely well for constant λ^{-1}. To simulate variations of λ^{-1} over time, we alter runs from the EM-GC that were conducted with constant λ^{-1}, by modifying the $\Delta T_{\mathrm{ATM,HUMAN}}$ component of these original EM-GC simulations. The value of λ^{-1} takes the same shape as the SSP4-3.4 RF time series, scaled, and shifted so that the new time series maintains an average value of λ^{-1} over the observational record that is identical to the constant λ^{-1} value. In simulations described below, the value of λ^{-1} is assumed to continue to rise into the future, at the same proportionality to $\Delta T_{\mathrm{ATM,HUMAN}}$ as the prior increase.

If we allow the value of λ^{-1} to scale with anthropogenic forcing such that the maximum value of χ^2_{ATM} is always less than or equal to 2, we obtain the result shown in Fig. 15b. This scaling of λ^{-1} results in a value of ΔT_{2100} about 50% higher than when a constant value of λ^{-1} is used and an increase in λ^{-1} by nearly a factor of 2.5 at the end of century. The modeled change in GMST starts to deviate from the observations around year 2000. This deviation is seen in the residual between modeled and observed GMST in Fig. 15f. If we allow the value of λ^{-1} to scale with anthropogenic forcing so that the maximum value of χ^2_{RECENT} is less than or equal to 2, we arrive at the result shown in Fig. 15c, yielding a value of ΔT_{2100} that nearly doubles over two and a half centuries and a rise in λ^{-1} by a factor of 4. The modeled change in GMST starts to deviate dramatically from observations around year 1990. This stark deviation is seen in the residual between modeled and observed GMST in Fig. 15g. The χ^2_{ATM} value in Fig. 15g is 3.63, which does not satisfy our reduced chi-squared constraints, and interestingly appears to resemble the behavior of some CMIP6 GCMs (see Fig. 9 as well as Tokarska et al. (2020)).

Several other studies have investigated the degree of change in λ^{-1}. Marvel et al. (2018) suggest that the median value of ECS from the CMIP5 GCMs may increase from 1.8 to 2.3°C or 1.8 to 3.1°C due to time varying λ^{-1}, which corresponds to an increase in λ^{-1} from 1850-2100 of 28 to 72%, respectively. Rugenstein et al. (2020) estimates a median increase of 17% for values of ECS from CMIP6 GCMs when examining millennial length simulations compared to the 150-year Gregory et al. (2004) method, which is consistent with about an 11% rise in λ^{-1} (Fig. 2b of Rugenstein et al. (2020)). A doubling (Fig. 15b) or quadrupling of λ^{-1} (Fig. 15c) over two and a half centuries is faster than the increase indicated by Marvel et al. (2018) and the millennia order timescale in Sect. 12.5.3 of IPCC 2013 and Rugenstein et al. (2020). A 50% increase or lower in λ^{-1} (Fig. 15d) is in line with the estimate of the change in ECS due to time-variant λ^{-1} indicated by Marvel et al. (2018) and Rugenstein et al. (2020). The assumption of constant feedback within the EM-GC framework is reasonable because there is no strong evidence from the climate record for a noticeable increase in λ^{-1} on the multidecadal simulations shown in Fig. 15. If the true value of λ^{-1} actually rises over time as suggested by some of the CMIP6 (Rugenstein et al., 2020) and CMIP5 GCMs (Marvel et al., 2018), our projections of global warming would be a few tenths of a degree warmer than our current best estimates assuming constant λ^{-1}, as shown in Fig. 15d. Interestingly, increasing λ^{-1} by 50% results in a similar value of ΔT_{2100} as when utilizing a higher value of AER RF_{2011} (i.e. AER RF_{2011} less than -0.9 W m^{-2}) in the EM-GC framework (see Fig. 3).

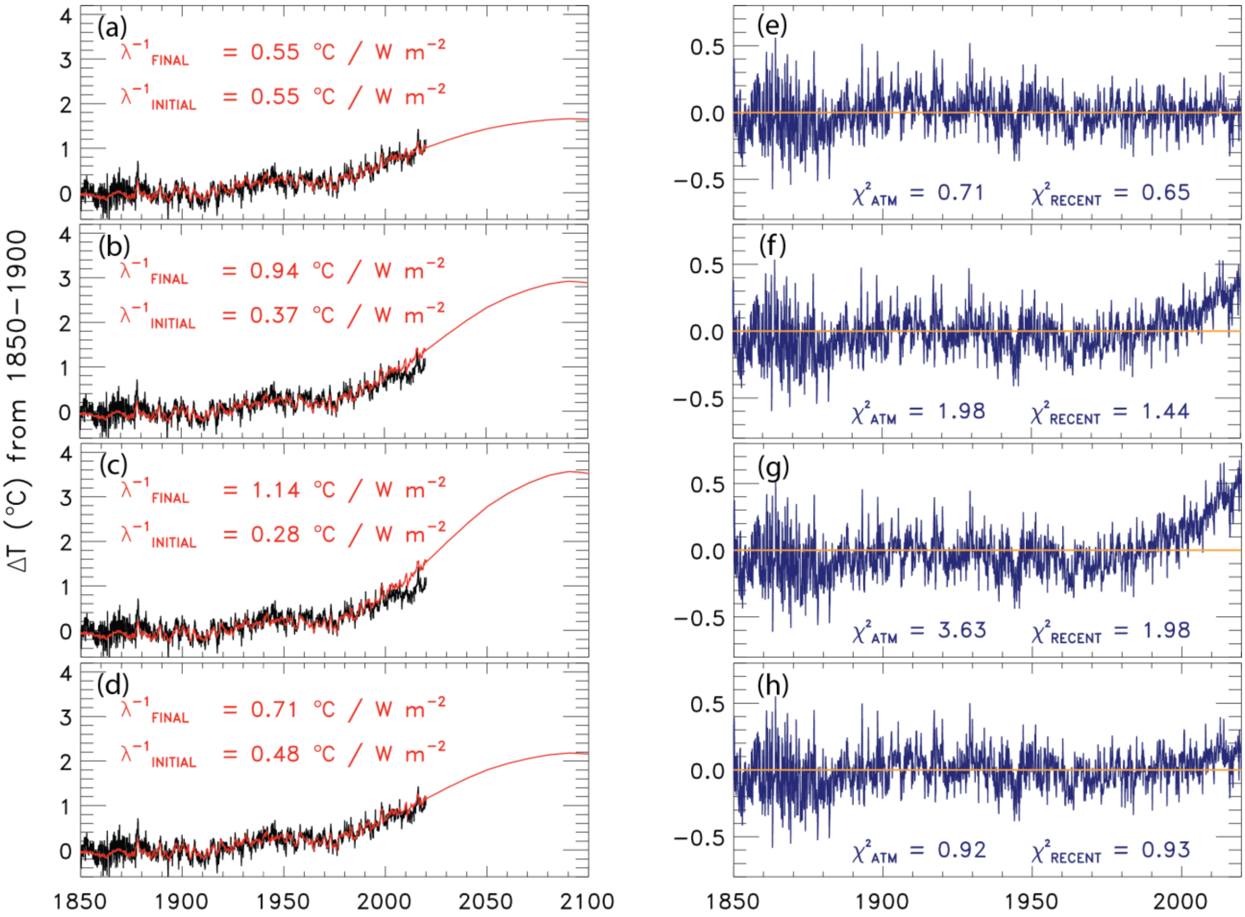

Figure 15. Change in GMST from 1850-2019 for observations from HadCRUT (black) and 1850-2100 for modeled (red) using SSP4-3.4 and the residual between modeled and observations. (a) Rise in GMST assuming a constant value of λ^{-1}. (b) Rise in GMST allowing λ^{-1} to vary while the value of χ^2_{ATM} is kept below 2. (c) Rise in GMST allowing λ^{-1} to vary while the value of χ^2_{RECENT} is kept below 2. (d) Rise in GMST allowing λ^{-1} to increase by 50%. (e) Residual between modeled and observed rise in GMST from 1850-2019 for constant λ^{-1}. (f) Same as (e) but for varying λ^{-1} while the value of χ^2_{ATM} is kept below 2. (g) Same as (f) but for varying λ^{-1} while the value of χ^2_{RECENT} is kept below 2. (h) same as (g) but for increasing λ^{-1} by 50%.

4 Conclusions

In this paper we use a multiple linear regression energy balance model (EM-GC), to analyze and project changes in the future rise in global mean surface temperature (GMST), calculate the attributable anthropogenic warming rate (AAWR, the component of the rise in GMST caused by human activities) over the past four decades, and compute the equilibrium climate sensitivity (ECS, the rise in GMST that would occur after climate has equilibrated with atmospheric CO_2 at the 2×pre-industrial level). Projections of the rise in GMST (ΔT) are conducted for seven of the Shared Socioeconomic Pathway (SSP) projections of GHGs (O'Neill et al., 2017). We compare computations of AAWR, ECS, and projections of ΔT to values for each quantity computed from archived output provided by GCMs as part of CMIP6 (Eyring et al., 2016). A critical component of our study is comprehensive analysis of uncertainties in AAWR, ECS, and projections of ΔT in our EM-GC framework, due to the rather large uncertainty in radiative forcing of climate from tropospheric aerosols (AER RF).

The best estimate of values of AAWR from 1975-2014 computed using our EM-GC constrained by the century and a half long record for GMST provided by the HadCRUT data record (Morice et al., 2012) is 0.135°C/decade and the 5th, and 95th percentiles are 0.097 and 0.195°C/decade, respectively. The median value of AAWR from the CMIP6 multi-model ensemble is 0.221°C/decade and the 5th, and 95th percentiles are 0.151 and 0.299°C/decade, respectively. We show that the component of GMST attributed to human activity within the CMIP6 multi-model ensemble warms considerably faster than observations over the past four decades, a result that is consistent with a recent analysis of output from the CMIP6 multi-model ensemble (Tokarska et al., 2020) as well as output from CMIP5 GCMs assessed in AR5 (i.e, Fig. 11.25b of Kirtman et al. (2013)). This finding differs from the conclusion of Hausfather et al. (2020), who showed fairly good agreement between projections of global warming from GCMs and observed ΔT. As detailed in Sect. 3.1, this paper examined GCMs that proceeded CMIP5 and examined ΔT for a time period that ends in 2017, a time when global temperature was influenced by a strong ENSO event that ended in 2016. The majority of the uncertainty in our EM-GC based estimate of AAWR is due to imprecise knowledge of the true value of AER RF.

In our model framework the best estimate of ECS is 2.01°C and the 5th and 95th percentiles are 1.12 and 4.12°C, respectively. The median value of ECS from the CMIP6 multi-model ensemble is 3.74°C, which is almost double the value of ECS inferred from the observed climate record. The 5th and 95th percentiles of ECS from the CMIP6 multi-model ensemble are 2.19 and 5.65°C, respectively. We obtain a wide range of ECS values using the EM-GC because of the uncertainty in AER RF. With an AER RF_{2011} equal to $-1.6\ W\ m^{-2}$, the EM-GC calculates a value of ECS similar to the maximum value of

ECS from the CMIP6 multi-model mean. We cannot rule out the very high value of ECS, but we assign a low probability based on the IPCC 2013 low likelihood for the needed value of AER RF_{2011}. Our empirically based determination of ECS is in good overall agreement with the recent empirical determinations of Lewis and Grünwald (2018) (1.87°C, range of 1.1-4.05°C) and Skeie et al. (2018) (2.0°C, range of 1.2-3.1°C) and the slightly older empirically determination reported by Otto et al. (2013) (2.0°C, range of 1.2-3.9°C) (all range values are for the 5th and 95th percent confidence interval). A recent review of climate feedback and climate sensitivity published by Sherwood et al. (2020) reported ECS lies within the range of 2.3 to 4.7°C at the 5th to 95th percent confidence intervals; their lower bound for ECS is quite a bit higher than the lower bound found in our analysis, as well as by Cox et al. (2018), Dessler et al. (2018), Lewis and Grünwald (2018), Nijsse et al. (2020), Otto et al. (2013), Skeie et al. (2018), and Tokarska et al. (2020).

We also examined the probability of limiting the future rise in GMST below the Paris Agreement target of 1.5°C and upper limit of 2.0°C. Our probabilistic forecasts of projections of ΔT include a comprehensive treatment of the uncertainty in AER RF, a capability outside the scope of the GCM intercomparisons conducted for CMIP6. Our analysis indicates that the SSP1-2.6 scenario is the 1.5°C pathway, providing between a 57.0-64.8% likelihood of keeping the end of century rise in ΔT below the Paris Agreement target of 1.5°C (relative to pre-industrial) depending on the choice of GMST and OHC record. We find that the SSP4-3.4 scenario is the 2.0°C pathway, as this scenario provides a 69.6-74.0% likelihood of limiting global warming to below the Paris Agreement upper limit of 2.0°C by end of century. In contrast, the CMIP6 multi-model mean only suggests a 15.2% probability of achieving the Paris Agreement target for SSP1-2.6 and a 16.7% probability of attaining the Paris Agreement goal for SSP4-3.4. This result is not surprising, given the tendency of most CMIP6 GCMs to warm faster than has been observed over the past four decades. Our projections of ΔT using a physically based model tied to observations of ocean heat content, quantification of natural as well as anthropogenic drivers of variations in GMST, and consideration of uncertainty in AER RF are shown to be remarkably similar to the expert assessment of the future rise in GMST that was sketched out in Fig. 11.25b of AR5 (Kirtman et al., 2013), and the empirically-based filtering of CMIP6 model output recently published by Tokarska et al. (2020).

Finally and most importantly, our estimates are based on the assumption that climate feedback has been and will continue to remain constant over time, since the prior temperature record can be fit so well under this assumption. As described in Section 3.3.6, if climate feedback rises over time, larger warming will be realized than that found under the assumption of temporally invariant feedback.

We also quantify the sensitivity of the probability of achieving the Paris Agreement target (1.5°C) or upper limit (2.0°C) to future atmospheric abundances of methane. The end of century mixing ratio of methane in the SSP1-2.6 scenario is 1.15 ppm, considerably less than the contemporary abundance of 1.88 ppm. The likelihood of attaining the 1.5°C target for SSP1-2.6 decreases as future methane emissions increase, declines to just under 50% if methane reaches 2.4 ppm in 2100 and to 34% if methane increases to 3.2 ppm at end of century. Our analysis described in Sect. 3.3.5 demonstrates that major near-term limits on the future growth of methane are especially important for achievement of the 1.5°C limit to future warming that constitutes the goal of the Paris Agreement.

Finally, we have also quantified in the EM-GC framework the remaining budgets of carbon (i.e., CO_2) emissions that can occur while attaining either the goal or upper limit of the Paris Agreement. We find that after 2019, society can only emit another 108 ± 75, 268 ± 91, or 336 ± 97 Gt C to have either a 95%, 66%, or 50% chance of limiting warming to 1.5°C. These future emissions estimates rise to 295 ± 93, 565 ± 120, and 685 ± 132 Gt C to have a 95%, 66%, or 50% chance of limiting warming to 2.0°C. Given the anthropogenic emissions of carbon due to combustion of fossil fuels, cement production, gas flaring, and land use change are about 11.7 Gt per year in 2019 (Friedlingstein et al., 2019), our study indicates that the target (1.5°C warming) of the Paris Agreement will not be achieved unless carbon emissions are severely curtailed in the next two decades.

We conclude by noting that the CMIP6 multi-model ensemble provides many useful parameters such as sea level rise, sea ice decline, and precipitation changes, that provide a great societal understanding of the impact of climate change. We do not mean to undermine the importance of the CMIP6 GCMs by this analysis. Rather, we hope that studies such as this, along with other recent evaluations of CMIP6 multi-model output such as Nijsse et al. (2020) and Tokarska et al. (2020) will provide improved use of the CMIP6 multi-model ensemble for policy decisions. Our EM-GC was built to specifically simulate and project changes in GMST; we do not examine numerous other components of the climate system that affect society. Our study indicates that unless society can implement steep reductions in the emissions of carbon (CO_2) and methane (CH_4) rather soon, the Paris Agreement will fail to be achieved. We suggest there is slighly more time to achieve these steep reductions than indicated by the CMIP6 multi-model mean. The incredibly valuable output of the CMIP6 GCMs is important for determining the consequences for society of 1.5°C, 2.0°C, or even larger rises in GMST.

5 Acronyms

AAWR – Attributable anthropogenic warming rate

AR4 – Fourth Assessment Report

AER – Anthropogenic aerosols

AER RF_{2011} – Radiative forcing due to anthropogenic aerosols in 2011

AMOC – Atlantic meridional overturning circulation

AMV – Atlantic multidecadal variability

BEG – Berkley Earth Group

CALIPSO – Cloud-Aerosol Lidar and Infrared Pathfinder Satellite Observations

CMIP5 – Coupled Model Intercomparison Project Phase 5

CMIP6 – Coupled Model Intercomparison Project Phase 6

COBE - Centennial in situ Observation-Based Estimate

CW14 – Cowtan and Way (2014) temperature record

ECS – Equilibrium climate sensitivity

EM-GC – Empirical Model of Global climate

ENSO – El Niño southern oscillation

GCM – General Circulation Model

GHG – Greenhouse gas

GISTEMP – Goddard Institute for Space Studies Surface Temperature Analysis v4

GloSSAC – Global Space-based Stratospheric Aerosol Climatology

GMST – Global mean surface temperature

HadCRUT – Hadley Center Climatic Research Unit

IPCC – Intergovernmental Panel on Climate Change

ISCCP – International Satellite Cloud Climatology Project

IOD – Indian Ocean dipole

LIN – Linear method

LUC – Land use change

MEI – Multivariate ENSO index

NOAAGT – National Center for Environmental Information NOAAGlobalTemp v5

ODS – Ozone depleting substances

OHC – Ocean heat content

OHE – Ocean heat export

PATMOS-X - Pathfinder Atmospheres Extended

PDO – Pacific decadal oscillation

RCP – Representative concentration pathway

REG – Regression method

RF – Radiative forcing

SAOD – Stratospheric aerosol optical depth

SORCE – Solar Radiation and Climate Experiment

SSP – Shared Socioeconomic Pathway

SST – Sea surface temperature

TAR – Third Assessment Report

TAS – Near surface air temperature

TCRE – Transient climate response to cumulative emissions

TOS – Temperature at the interface of the atmosphere and the upper boundary of the ocean

TSI – Total solar irradiance

6 Author Contribution

LAM, APH, and TPC developed the model code used in this analysis, LAM, APH, and BFB collected data, RJS supervised, administrated, and developed the project, LAM wrote the original draft, and RJS, APH, BFB, TPC, and WRT participated in the review and editing of the manuscript.

7 Competing Interests

The authors declare that they have no conflict of interest.

8 Acknowledgements

We would like to acknowledge the World Climate Research Programme for coordinating and promoting CMIP6 through its Working Group on Coupled Modelling. We thank the climate modeling groups participating in CMIP6 for producing and making their model results available, the Earth System Grid Federation (ESGF) for archiving the data and providing access, and the several funding agencies who support ESGF and CMIP6. This project could not occur without the results from CMIP6. We appreciate very much financial support from the NASA Climate Indicators and Data Products for Future National Climate Assessments (INCA) program (award NNX16AG34G). This study was partially supported by NOAA grants NA14NES4320003 and NA19NES4320002 (Cooperative Institute for Satellite Earth System Studies - CISESS) at the University of Maryland/ESSIC. We thank University of Maryland Undergraduate Lauren Borgia for participating in extensive, in-depth discussions of recent papers on cloud feedback and climate sensitivity. Finally, we thank both reviewers for very careful reads of the original paper that led to substantial improvements in the manuscript, as well as Martin Stolpe for contacting us privately, while the paper was in discussion, regarding an erroneous description of the effect of creating blended near surface air temperature that had appeared in the submitted paper.

9 References

Arfeuille, F., Weisenstein, D., MacK, H., Rozanov, E., Peter, T. and Brönnimann, S.: Volcanic forcing for climate modeling: A new microphysics-based data set covering years 1600-present, Clim. Past, 10(1), 359–375, doi:10.5194/cp-10-359-2014, 2014.

Armour, K. C.: Energy budget constraints on climate sensitivity in light of inconstant climate feedbacks, Nat. Clim. Chang., 7(5), 331–335, doi:10.1038/nclimate3278, 2017.

Balmaseda, M. A., Trenberth, K. E. and Källén, E.: Distinctive climate signals in reanalysis of global ocean heat content, Geophys. Res. Lett., 40(9), 1754–1759, doi:10.1002/grl.50382, 2013.

Barnett, T. P., Pierce, D. W., Latif, M., Dommenget, D. and Saravan, R.: Interdecadal interactions between the tropics and midlatitudes in the Pacific basin, Geophys. Res. Lett., 26(5), 615–618, 1999.

Bond, T. C., Doherty, S. J., Fahey, D. W., Forster, P. M., Berntsen, T., Deangelo, B. J., Flanner, M. G., Ghan, S., Kärcher, B., Koch, D., Kinne, S., Kondo, Y., Quinn, P. K., Sarofim, M. C., Schultz, M. G., Schulz, M., Venkataraman, C., Zhang, H., Zhang, S., Bellouin, N., Guttikunda, S. K., Hopke, P. K., Jacobson, M. Z., Kaiser, J. W., Klimont, Z., Lohmann, U., Schwarz, J. P., Shindell, D., Storelvmo, T., Warren, S. G. and Zender, C. S.: Bounding the role of black carbon in the climate system: A scientific assessment, J. Geophys. Res. Atmos., 118(11), 5380–5552, doi:10.1002/jgrd.50171, 2013.

Bony, S., Colman, R., Kattsov, V. M., Allan, R. P., Bretherton, C. S., Dufresne, J. L., Hall, A., Hallegatte, S., Holland, M. M., Ingram, W., Randall, D. A., Soden, B. J., Tselioudis, G. and Webb, M. J.: How well do we understand and evaluate climate change feedback processes?, J. Clim., 19(15), 3445–3482, doi:10.1175/JCLI3819.1, 2006.

Calvin, K., Bond-Lamberty, B., Clarke, L., Edmonds, J., Eom, J., Hartin, C., Kim, S., Kyle, P., Link, R., Moss, R., McJeon, H., Patel, P., Smith, S., Waldhoff, S. and Wise, M.: The SSP4: A world of deepening inequality, Glob. Environ. Chang., 42, 284–296, doi:10.1016/j.gloenvcha.2016.06.010, 2017.

Canty, T., Mascioli, N. R., Smarte, M. D. and Salawitch, R. J.: An empirical model of global climate – Part 1: A critical evaluation of volcanic cooling, Atmos. Chem. Phys., 13(8), 3997–4031, doi:10.5194/acp-13-3997-2013, 2013.

Carpenter, L. J., Daniel, J. S. (Lead A., Fleming, E. L., Hanaoka, T., Ravishankara, A. R., Ross, M. N., Tilmes, S., Wallington, T. J. and Wuebbles, D. J.: Scenarios and information for policymakers., 2018.

Carton, J. A., Chepurin, G. A. and Chen, L.: SODA3: A New Ocean Climate Reanalysis, J. Clim., 31(17), 6967–6983, doi:10.1175/jcli-d-18-0149.1, 2018.

Charette, M. A. and Smith, W. H. F.: The Volume of Earth ' s Ocean, Oceanography, 23(2), 112–114, 2010.

Chen, X. and Tung, K. K.: Global surface warming enhanced by weak Atlantic overturning circulation, Nature, 559(7714), 387–391, doi:10.1038/s41586-018-0320-y, 2018.

Chen, X., Guo, Z., Zhou, T., Li, J., Rong, X., Xin, Y., Chen, H. and Su, J.: Climate Sensitivity and Feedbacks of a New Coupled Model CAMS-CSM to Idealized CO2 Forcing: A Comparison with CMIP5 Models, J. Meteorol. Res., 33(1), 31–45, doi:10.1007/s13351-019-8074-5, 2019.

Cheng, L., Trenberth, K. E., Fasullo, J., Boyer, T., Abraham, J. and Zhu, J.: Improved estimates of ocean heat content from 1960 to 2015, Sci. Adv., 3(3), 1–11, doi:10.1126/sciadv.1601545, 2017.

Church, J. A., White, N. J., Konikow, L. F., Domingues, C. M., Graham Cogley, J., Rignot, E., Gregory, J. M., Van Den Broeke, M. R., Monaghan, A. J. and Velicogna, I.: Revisiting the Earth's sea-level and energy budgets from 1961 to 2008, Geophys. Res. Lett., 40(15), 4066, doi:10.1002/grl.50752, 2013.

Cowtan, K. and Way, R. G.: Coverage bias in the HadCRUT4 temperature series and its impact on recent temperature trends, Q. J. R. Meteorol. Soc., 140(683), 1935–1944, doi:10.1002/qj.2297, 2014.

Cowtan, K., Hausfather, Z., Hawkins, E., Jacobs, P., Mann, M. E., Miller, S. K., Steinman, B. A., Stolpe, M. B. and Way, R. G.: Robust comparison of climate models with observations using blended land air and ocean sea surface temperatures, Geophys. Res. Lett., 42(15), 6526–6534, doi:10.1002/2015GL064888, 2015.

Cox, P. M., Huntingford, C. and Williamson, M. S.: Emergent constraint on equilibrium climate sensitivity from global temperature variability, Nature, 553(7688), 319–322, doi:10.1038/nature25450, 2018.

Dessler, A. E., Mauritsen, T. and Stevens, B.: The influence of internal variability on Earth's energy balance framework and implications for estimating climate sensitivity, Atmos. Chem. Phys., 18(7), 5147–5155, doi:10.5194/acp-18-5147-2018, 2018.

Dlugokencky, E.: Trends in Atmospheric Methane, [online] Available from: www.esrl.noaa.gov/gmd/ccgg/trends_ch4/, 2020.

Dlugokencky, E. and Tans, P.: Trends in Atmospheric Carbon Dioxide, [online] Available from: www.esrl.noaa.gov/gmd/ccgg/trends/, 2020.

Domingues, C. M., Church, J. A., White, N. J., Gleckler, P. J., Wijffels, S. E., Barker, P. M. and Dunn, J. R.: Improved estimates of upper-ocean warming and multi-decadal sea-level rise, Nature, 453(7198), 1090–1093, doi:10.1038/nature07080, 2008.

Douglass, D. H. and Knox, R. S.: Climate forcing by the volcanic eruption of Mount Pinatubo, Geophys. Res. Lett., 32(5), 1–5, doi:10.1029/2004GL022119, 2005.

Dudok de Wit, T., Kopp, G., Fröhlich, C. and Schöll, M.: Methodology to create a new total solar irradiance record: Making a composite out of multiple data records, Geophys. Res. Lett., 44(3), 1196–1203, doi:10.1002/2016GL071866, 2017.

England, M. H., Mcgregor, S., Spence, P., Meehl, G. A., Timmermann, A., Cai, W., Gupta, A. Sen, Mcphaden, M. J., Purich, A. and Santoso, A.: Recent intensification of wind-driven circulation in the Pacific and the ongoing warming hiatus, Nat. Clim. Chang., 4(3), 222–227, doi:10.1038/nclimate2106, 2014.

Eyring, V., Bony, S., Meehl, G. A., Senior, C. A., Stevens, B., Stouffer, R. J. and Taylor, K. E.: Overview of the Coupled Model Intercomparison Project Phase 6 (CMIP6) experimental design and organization, Geosci. Model Dev., 9(5), 1937–1958, doi:10.5194/gmd-9-1937-2016, 2016.

Forster, P. M., Maycock, A. C., McKenna, C. M. and Smith, C. J.: Latest climate models confirm need for urgent mitigation, Nat. Clim. Chang., 10(1), 7–10, doi:10.1038/s41558-019-0660-0, 2020.

Foster, G. and Rahmstorf, S.: Global temperature evolution 1979–2010, Environ. Res. Lett., 6(4), 044022, doi:10.1088/1748-9326/6/4/044022, 2011.

Foster, M. J. and Heidinger, A.: PATMOS-x: Results from a diurnally corrected 30-yr satellite cloud climatology, J. Clim., 26(2), 414–425, doi:10.1175/JCLI-D-11-00666.1, 2013.

Fricko, O., Havlik, P., Rogelj, J., Klimont, Z., Gusti, M., Johnson, N., Kolp, P., Strubegger, M., Valin, H., Amann, M., Ermolieva, T., Forsell, N., Herrero, M., Heyes, C., Kindermann, G., Krey, V., McCollum, D. L., Obersteiner, M., Pachauri, S., Rao, S., Schmid, E., Schoepp, W. and Riahi, K.: The marker quantification of the Shared Socioeconomic Pathway 2: A middle-of-the-road scenario for the 21st century, Glob. Environ. Chang., 42, 251–267, doi:10.1016/j.gloenvcha.2016.06.004, 2017.

Friedlingstein, P., Meinshausen, M., Arora, V. K., Jones, C. D., Anav, A., Liddicoat, S. K. and Knutti, R.: Uncertainties in CMIP5 climate projections due to carbon cycle feedbacks, J. Clim., 27(2), 511–526, doi:10.1175/JCLI-D-12-00579.1, 2014.

Friedlingstein, P., Jones, M. W., Sullivan, M. O., Andrew, R. M., Hauck, J., Peters, G. P., Peters, W., Pongratz, J., Sitch, S., Quéré, C. Le, Bakker, D. C. E., Canadell, J. G., Ciais, P., Jackson, R. B., Anthoni, P., Barbero, L., Bastos, A., Bastrikov, V., Becker, M., Bopp, L., Buitenhuis, E., Chandra, N., Chevallier, F., Chini, L. P., Currie, K., Feely, R. A., Gehlen, M., Gilfillan, D., Gkritzalis, T., Goll, D. S., Gruber, N., Gutekunst, S., Harris, I., Haverd, V., Houghton, R. A., Hurtt, G., Ilyina, T., Jain, A. K., Joetzjer, E., Kaplan, J. O., Kato, E., Goldewijk, K. K., Korsbakken, J. I., Landschützer, P., Lauvset, S. K., Lefevre, N., Lenton, A., Lienert, S., Lombardozzi, D., Marland, G., McGuire, P. C., Melton, J. R., Metzl, N., Munro, D. R., Nabel, J. E. M. S., Nakaoka, S., Neill, C., Omar, A. M., Ono, T., Peregon, A., Pierrot, D., Poulter, B., Rehder, G., Resplandy, L., Robertson, E., Rodenbeck, C., Seferian, R., Schwinger, J., Smith, N., Tans, P. P., Tian, H., Tilbrook, B., Tubiello, F. N., Van Der Werf, G. R., Wiltshire, A. J. and Zaehle, S.: Global Carbon Budget 2019, Earth Syst. Sci. Data, (11), 1783–1838, 2019.

Fujimori, S., Hasegawa, T., Masui, T., Takahashi, K., Herran, D. S., Dai, H., Hijioka, Y. and Kainuma, M.: SSP3: AIM implementation of Shared Socioeconomic Pathways, Glob. Environ. Chang., 42, 268–283, doi:10.1016/j.gloenvcha.2016.06.009, 2017.

Gettelman, A., Hannay, C., Bacmeister, J. T., Neale, R. B., Pendergrass, A. G., Danabasoglu, G., Lamarque, J. F., Fasullo, J. T., Bailey, D. A., Lawrence, D. M. and Mills, M. J.: High Climate Sensitivity in the Community Earth System Model Version 2 (CESM2), Geophys. Res. Lett., 46(14), 8329–8337, doi:10.1029/2019GL083978, 2019.

Gregory, J. M.: Vertical heat transports in the ocean and their effect on time-dependent climate change, Clim. Dyn., 16(7), 501–515, doi:10.1007/s003820000059, 2000.

Gregory, J. M., Ingram, W. J., Palmer, M. A., Jones, G. S., Stott, P. A., Thorpe, R. B., Lowe, J. A., Johns, T. C. and Williams, K. D.: A new method for diagnosing radiative forcing and climate sensitivity, Geophys. Res. Lett., 31(3), 2–5, doi:10.1029/2003GL018747, 2004.

Griffies, S. M., Danabasoglu, G., Durack, P. J., Adcroft, A. J., Balaji, V., Böning, C. W., Chassignet, E. P., Curchitser, E., Deshayes, J., Drange, H., Fox-Kemper, B., Gleckler, P. J., Gregory, J. M., Haak, H., Hallberg, R. W., Heimbach, P., Hewitt, H. T., Holland, D. M., Ilyina, T., Jungclaus, J. H., Komuro, Y., Krasting, J. P., Large, W. G., Marsland, S. J., Masina, S., McDougall, T. J., George Nurser, A. J., Orr, J. C., Pirani, A., Qiao, F., Stouffer, R. J., Taylor, K. E., Treguier, A. M., Tsujino, H., Uotila, P., Valdivieso, M., Wang, Q., Winton, M. and Yeager, S. G.: OMIP contribution to CMIP6: Experimental and diagnostic protocol for the physical component of the Ocean Model Intercomparison Project, Geosci. Model Dev., 9(9), 3231–3296, doi:10.5194/gmd-9-3231-2016, 2016.

Hansen, J., Ruedy, R., Sato, M. and Lo, K.: Global surface temperature change, Rev. Geophys., 48(4), RG4004, doi:10.1029/2010RG000345.1.INTRODUCTION, 2010.

Hausfather, Z., Drake, H. F., Abbott, T. and Schmidt, G. A.: Evaluating the Performance of Past Climate Model Projections, Geophys. Res. Lett., 47(1), 0–3, doi:10.1029/2019GL085378, 2020.

Haustein, K., Otto, F. E. L., Venema, V., Jacobs, P., Cowtan, K., Hausfather, Z., Way, R. G., White, B., Subramanian, A. and Schurer, A. P.: A limited role for unforced internal variability in twentieth-century warming, J. Clim., 32(16), 4893–4917, doi:10.1175/JCLI-D-18-0555.1, 2019.

Hope, A. P., Canty, T. P., Salawitch, R. J., Tribett, W. R. and Bennett, B. F.: Forecasting Global Warming, in Paris Climate Agreement: Beacon of Hope, pp. 51–114, Springer Climate., 2017.

Ishii, M., Shouji, A., Sugimoto, S. and Matsumoto, T.: Objective analyses of sea-surface temperature and marine meteorological variables for the 20th century using ICOADS and the Kobe Collection, Int. J. Climatol., 25(7), 865–879, doi:10.1002/joc.1169, 2005.

Ishii, M., Fukuda, Y., Hirahara, S., Yasui, S., Suzuki, T. and Sato, K.: Accuracy of Global Upper Ocean Heat Content Estimation Expected from Present Observational Data Sets, Sci. Online Lett. Atmos., 13(0), 163–167, doi:10.2151/sola.2017-030, 2017.

Jackson, L. C., Kahana, R., Graham, T., Ringer, M. A., Woollings, T., Mecking, J. V. and Wood, R. A.: Global and European climate impacts of a slowdown of the AMOC in a high resolution GCM, Clim. Dyn., 45(11–12), 3299–3316, doi:10.1007/s00382-015-2540-2, 2015.

Jones, C., Sellar, A., Tang, Y. and Rumbold, S.: Results from the UKESM1 CMIP6 DECK and historical simulations, UKESM [online] Available from: https://ukesm.ac.uk/portfolio-item/ukesm1-cmip6-deck-and-historical/# (Accessed 9 October 2019), 2019.

Kavvada, A., Ruiz-Barradas, A. and Nigam, S.: AMO's structure and climate footprint in observations and IPCC AR5 climate simulations, Clim. Dyn., 41(5–6), 1345–1364, doi:10.1007/s00382-013-1712-1, 2013.

Kennedy, J. J., Rayner, N. A., Smith, R. O., Parker, D. E. and Saunby, M.: Reassessing biases and other uncertainties in sea surface temperature observations measured in situ since 1850: 2. Biases and homogenization, J. Geophys. Res., 116(D14), 1–22, doi:10.1029/2010jd015220, 2011.

Kiehl, J. T.: Twentieth century climate model response and climate sensitivity, Geophys. Res. Lett., 34(22), 1–4, doi:10.1029/2007GL031383, 2007.

Kirschke, S., Bousquet, P., Ciais, P., Saunois, M., Canadell, J. G., Dlugokencky, E. J., Bergamaschi, P., Bergmann, D., Blake, D. R., Bruhwiler, L., Cameron-Smith, P., Castaldi, S., Chevallier, F., Feng, L., Fraser, A., Heimann, M., Hodson, E. L., Houweling, S., Josse, B., Fraser, P. J., Krummel, P. B., Lamarque, J. F., Langenfelds, R. L., Le Quéré, C., Naik, V., O'doherty, S., Palmer, P. I., Pison, I., Plummer, D., Poulter, B., Prinn, R. G., Rigby, M., Ringeval, B., Santini, M., Schmidt, M., Shindell, D. T., Simpson, I. J., Spahni, R., Steele, L. P., Strode, S. A., Sudo, K., Szopa, S., Van Der Werf, G. R., Voulgarakis, A., Van Weele, M., Weiss, R. F., Williams, J. E. and Zeng, G.: Three decades of global methane sources and sinks, Nat. Geosci., 6(10), 813–823, doi:10.1038/ngeo1955, 2013.

Kirtman, B., Power, S. B., Adedoyin, A. J., Boer, G. J., Bojariu, R., Camilloni, I., Doblas-Reyes, F., Fiore, A. M., Kimoto, M., Meehl, G., Prather, M., Sarr, A., Schär, C., Sutton, R., van Oldenborgh, G. J., Vecchi, G. and Wang, H. J.: Near-term climate change: Projections and predictability, Clim. Chang. 2013 Phys. Sci. Basis Work. Gr. I Contrib. to Fifth Assess. Rep. Intergov. Panel Clim. Chang., 9781107057, 953–1028, doi:10.1017/CBO9781107415324.023, 2013.

Klein, S. A., Hall, A., Norris, J. R. and Pincus, R.: Low-Cloud Feedbacks from Cloud-Controlling Factors: A Review, Surv. Geophys., 38(6), 1307–1329, doi:10.1007/s10712-017-9433-3, 2017.

Knight, J. R., Allan, R. J., Folland, C. K., Vellinga, M. and Mann, M. E.: A signature of persistent natural thermohaline circulation cycles in observed climate, Geophys. Res. Lett., 32(20), 1–4, doi:10.1029/2005GL024233, 2005.

Kriegler, E., Weyant, J. P., Blanford, G. J., Krey, V., Clarke, L., Edmonds, J., Fawcett, A., Luderer, G., Riahi, K., Richels, R., Rose, S. K., Tavoni, M. and van Vuuren, D. P.: The role of technology for achieving climate policy objectives: Overview of the EMF 27 study on global technology and climate policy strategies, Clim. Change, 123(3–4), 353–367, doi:10.1007/s10584-013-0953-7, 2014.

Kriegler, E., Riahi, K., Bauer, N., Schwanitz, V. J., Petermann, N., Bosetti, V., Marcucci, A., Otto, S., Paroussos, L., Rao, S., Arroyo Currás, T., Ashina, S., Bollen, J., Eom, J., Hamdi-Cherif, M., Longden, T., Kitous, A., Méjean, A., Sano, F., Schaeffer, M., Wada, K., Capros, P., P. van Vuuren, D. and Edenhofer, O.: Making or breaking climate targets: The AMPERE study on staged accession scenarios for climate policy, Technol. Forecast. Soc. Change, doi:10.1016/j.techfore.2013.09.021, 2015.

Kriegler, E., Bauer, N., Popp, A., Humpenöder, F., Leimbach, M., Strefler, J., Baumstark, L., Bodirsky, B. L., Hilaire, J., Klein, D., Mouratiadou, I., Weindl, I., Bertram, C., Dietrich, J. P., Luderer, G., Pehl, M., Pietzcker, R., Piontek, F., Lotze-Campen, H., Biewald, A., Bonsch, M., Giannousakis, A., Kreidenweis, U., Müller, C., Rolinski, S., Schultes, A., Schwanitz, J., Stevanovic, M., Calvin, K., Emmerling, J., Fujimori, S. and Edenhofer, O.: Fossil-fueled development (SSP5): An energy and resource intensive scenario for the 21st century, Glob. Environ. Chang., 42, 297–315, doi:10.1016/j.gloenvcha.2016.05.015, 2017.

Kushnir, Y.: Interdecadal Variations in North Atlantic Sea Surface Temperature and Associated Atmospheric Conditions, J. Clim., 7(1), 141–157, doi:10.1175/1520-0442(1994)007<0141:IVINAS>2.0.CO;2, 1994.

Lean, J. L. and Rind, D. H.: How natural and anthropogenic influences alter global and regional surface temperatures: 1889 to 2006, Geophys. Res. Lett., 35(18), 1–6, doi:10.1029/2008GL034864, 2008.

Lean, J. L. and Rind, D. H.: How will Earth’s surface temperature change in future decades?, Geophys. Res. Lett., 36(15), 1–5, doi:10.1029/2009GL038932, 2009.

Lelieveld, J., Evans, J. S., Fnais, M., Giannadaki, D. and Pozzer, A.: The contribution of outdoor air pollution sources to premature mortality on a global scale, Nature, 525(7569), 367–371, doi:10.1038/nature15371, 2015.

Levitus, S., Antonov, J. I., Boyer, T. P., Baranova, O. K., Garcia, H. E., Locarnini, R. A., Mishonov, A. V., Reagan, J. R., Seidov, D., Yarosh, E. S. and Zweng, M. M.: World ocean heat content and thermosteric sea level change (0-2000m), 1955-2010, Geophys. Res. Lett., 39(10), 1–5, doi:10.1029/2012GL051106, 2012.

Lewis, N. and Curry, J.: The impact of recent forcing and ocean heat uptake data on estimates of climate sensitivity, J. Clim., 31(15), 6051–6071, doi:10.1175/JCLI-D-17-0667.1, 2018.

Lewis, N. and Grünwald, P.: Objectively combining AR5 instrumental period and paleoclimate climate sensitivity evidence, Clim. Dyn., 50(5), 2199–2216, doi:10.1007/s00382-017-3744-4, 2018.

Liang, Y., Gillett, N. P. and Monahan, A. H.: Climate Model Projections of 21st Century Global Warming Constrained Using the Observed Warming Trend, Geophys. Res. Lett., 47(12), 1–10, doi:10.1029/2019GL086757, 2020.

Marvel, K., Pincus, R., Schmidt, G. A. and Miller, R. L.: Internal Variability and Disequilibrium Confound Estimates of Climate Sensitivity From Observations, Geophys. Res. Lett., 45(3), 1595–1601, doi:10.1002/2017GL076468, 2018.

Mascioli, N. R., Canty, T. and Salawitch, R. J.: An empirical model of global climate – Part 2: Implications for future temperature, Atmos. Chem. Phys., 2013.

Matthes, K., Funke, B., Andersson, M. E., Barnard, L., Beer, J., Charbonneau, P., Clilverd, M. A., Dudok de Wit, T., Haberreiter, M., Hendry, A., Jackman, C. H., Kretzschmar, M., Kruschke, T., Kunze, M., Langematz, U., Marsh, D. R., Maycock, A. C., Misios, S., Rodger, C. J., Scaife, A. A., Seppala, A., Shangguan, M., Sinnhuber, M., Tourpali, K., Usoskin, I., van de Kamp, M., Verronen, P. T. and Versick, S.: Solar forcing for CMIP6 (v3.2), Geosci. Model Dev., 10, 2247–2302, 2017.

McBride, L. A., Hope, A. P., Canty, T. P., Bennett, B. F., Tribett, W. R. and Salawitch, R. J.: Input and Output Files EMGC, , doi:10.5281/zenodo.3908407, 2020.

Medhaug, I. and Furevik, T.: North Atlantic 20th century multidecadal variability in coupled climate models: Sea surface temperature and ocean overturning circulation, Ocean Sci., 7(3), 389–404, doi:10.5194/os-7-389-2011, 2011.

Meehl, G. A., Senior, C. A., Eyring, V., Flato, G., Lamarque, J. F., Stouffer, R. J., Taylor, K. E. and Schlund, M.: Context for interpreting equilibrium climate sensitivity and transient climate response from the CMIP6 Earth system models, Sci. Adv., 6(26), 1–11, doi:10.1126/sciadv.aba1981, 2020.

Meinshausen, M., Smith, S. J., Calvin, K., Daniel, J. S., Kainuma, M. L. T., Lamarque, J., Matsumoto, K., Montzka, S. A., Raper, S. C. B., Riahi, K., Thomson, A., Velders, G. J. M. and van Vuuren, D. P. P.: The RCP greenhouse gas concentrations and their extensions from 1765 to 2300, Clim. Change, 109(1), 213–241, doi:10.1007/s10584-011-0156-z, 2011.

Meinshausen, M., Vogel, E., Nauels, A., Lorbacher, K., Meinshausen, N., Etheridge, D. M., Fraser, P. J., Montzka, S. A., Rayner, P. J., Trudinger, C. M., Krummel, P. B., Beyerle, U., Canadell, J. G., Daniel, J. S., Enting, I. G., Law, R. M., Lunder, C. R., O’Doherty, S., Prinn, R. G., Reimann, S., Rubino, M., Velders, G. J. M., Vollmer, M. K., Wang, R. H. J. and Weiss, R.: Historical greenhouse gas concentrations for climate modelling (CMIP6), Geosci. Model Dev., 10(5), 2057–2116, doi:10.5194/gmd-10-2057-2017, 2017.

Millar, R. J., Fuglestvedt, J. S., Friedlingstein, P., Rogelj, J., Grubb, M. J., Matthews, H. D., Skeie, R. B., Forster, P. M., Frame,

D. J. and Allen, M. R.: Emission budgets and pathways consistent with limiting warming to 1.5°C, Nat. Geosci., 11(6), 454–455, doi:10.1038/s41561-018-0153-1, 2017.

Morice, C. P., Kennedy, J. J., Rayner, N. A. and Jones, P. D.: Quantifying uncertainties in global and regional temperature change using an ensemble of observational estimates: The HadCRUT4 data set, J. Geophys. Res. Atmos., 117(8), 1–22, doi:10.1029/2011JD017187, 2012.

Murphy, J. M., Booth, B. B. B., Boulton, C. A., Clark, R. T., Harris, G. R., Lowe, J. A. and Sexton, D. M. H.: Transient climate changes in a perturbed parameter ensemble of emissions-driven earth system model simulations, Clim. Dyn., 43(9–10), 2855–2885, doi:10.1007/s00382-014-2097-5, 2014.

Myhre, G., Highwood, E. J., Shine, K. P. and Stordal, F.: New estimates of radiative forcing due to wel mixed greenhouse gases, Geophys. Res. Lett., 25(14), 2715–2718, 1998.

Myhre, G., Nilsen, J. S., Gulstad, L., Shine, K. P., Rognerud, B. and Isaksen, I. S. A.: Radiative forcing due to stratospheric water vapour from CH4 oxidation, Geophys. Res. Lett., 34(1), 3–7, doi:10.1029/2006GL027472, 2007.

Myhre, G., Shindell, D., Bréon, F.-M., Collins, W., Fuglestvedt, J., Huang, J., Koch, D., Lamarque, J.-F., Lee, D., Mendoza, B., Nakajima, T., Robock, A., Stephens, G., Takemura, T. and Zhang, H.: Anthropogenic and Natural Radiative Forcing, Clim. Chang. 2013 Phys. Sci. Basis. Contrib. Work. Gr. I to Fifth Assess. Rep. Intergov. Panel Clim. Chang., 659–740, doi:10.1017/ CBO9781107415324.018, 2013.

Nicholls, Z., Meinshausen, M., Lewis, J., Corradi, M. R., Dorheim, K., Gasser, T., Gieseke, R., Hope, A. P., Leach, N. J., McBride, L. A., Quilcaille, Y., Rogelj, J., Salawitch, R. J., Samset, B. H., Sandstad, M., Shiklomanov, A., Skeie, R. B., Smith, C. J., Smith, S. J., Su, X., Tsutsui, J., Vega-Westhoff, B. and Woodward, D.: Reduced Complexity Model Intercomparison Project Phase 2 : Synthesising Earth system knowledge for probabilistic climate projections, Earth's Futur., doi:https://doi.org/10.1002/essoar.10504793.1, 2020a.

Nicholls, Z. R. J., Meinshausen, M., Lewis, J., Gieseke, R., Dommenget, D., Dorheim, K., Fan, C.-S., Fuglestvedt, J. S., Gasser, T., Golüke, U., Goodwin, P., Hartin, C., Hope, A. P., Kriegler, E., Leach, N. J., Marchegiani, D., McBride, L. A., Quilcaille, Y., Rogelj, J., Salawitch, R. J., Samset, B. H., Sandstad, M., Shiklomanov, A. N., Skeie, R. B., Smith, C. J., Smith, S., Tanaka, K., Tsutsui, J. and Xie, Z.: Reduced Complexity Model Intercomparison Project Phase 1: introduction and evaluation of global-mean temperature response, Geosci. Model Dev., 13(11), 5175–5190, doi:10.5194/gmd-13-5175-2020, 2020b.

Nigam, S., Guan, B. and Ruiz-Barradas, A.: Key role of the Atlantic Multidecadal Oscillation in 20th century drought and wet periods over the Great Plains, Geophys. Res. Lett., 38(16), 1–6, doi:10.1029/2011GL048650, 2011.

Nijsse, F. J. M. M., Cox, P. M. and Williamson, M. S.: Emergent constraints on transient climate response (TCR) and equilibrium climate sensitivity (ECS) from historical warming in CMIP5 and CMIP6 models, Earth Syst. Dyn., 11, 737–750, 2020.

O'Neill, B. C., Kriegler, E., Riahi, K., Ebi, K. L., Hallegatte, S., Carter, T. R., Mathur, R. and van Vuuren, D. P.: A new scenario framework for climate change research: The concept of shared socioeconomic pathways, Clim. Change, 122(3), 387–400, doi:10.1007/s10584-013-0905-2, 2014.

O'Neill, B. C., Tebaldi, C., Van Vuuren, D. P., Eyring, V., Friedlingstein, P., Hurtt, G., Knutti, R., Kriegler, E., Lamarque, J. F., Lowe, J., Meehl, G. A., Moss, R., Riahi, K. and Sanderson, B. M.: The Scenario Model Intercomparison Project (ScenarioMIP) for CMIP6, Geosci. Model Dev., 9(9), 3461–3482, doi:10.5194/gmd-9-3461-2016, 2016.

O'Neill, B. C., Kriegler, E., Ebi, K. L., Kemp-Benedict, E., Riahi, K., Rothman, D. S., van Ruijven, B. J., van Vuuren, D. P., Birkmann, J., Kok, K., Levy, M. and Solecki, W.: The roads ahead: Narratives for shared socioeconomic pathways describing world futures in the 21st century, Glob. Environ. Chang., 42, 169–180, doi:10.1016/j.gloenvcha.2015.01.004, 2017.

Otto, A., Otto, F. E. L., Boucher, O., Church, J., Hegerl, G., Forster, P. M., Gillett, N. P., Gregory, J., Johnson, G. C., Knutti, R., Lewis, N., Lohmann, U., Marotzke, J., Myhre, G., Shindell, D., Stevens, B. and Allen, M. R.: Energy budget constraints on climate response, Nat. Geosci., 6(6), 415–416, doi:10.1038/ngeo1836, 2013.

Proistosescu, C. and Huybers, P. J.: Slow climate mode reconciles historical and model-based estimates of climate sensitivity, Sci. Adv., 3(7), 1–7, doi:10.1126/sciadv.1602821, 2017.

Raper, S. C. B., Gregory, J. M. and Stouffer, R. J.: The role of climate sensitivity and ocean heat uptake on AOGCM transient temperature response, J. Clim., 15(1), 124–130, doi:10.1175/1520-0442(2002)015<0124:TROCSA>2.0.CO;2, 2002.

Riahi, K., Kriegler, E., Johnson, N., Bertram, C., den Elzen, M., Eom, J., Schaeffer, M., Edmonds, J., Isaac, M., Krey, V., Longden, T., Luderer, G., Méjean, A., McCollum, D. L., Mima, S., Turton, H., van Vuuren, D. P., Wada, K., Bosetti, V., Capros, P., Criqui, P., Hamdi-Cherif, M., Kainuma, M. and Edenhofer, O.: Locked into Copenhagen pledges - Implications of short-term emission targets for the cost and feasibility of long-term climate goals, Technol. Forecast. Soc. Change, 90(PA), 8–23, doi:10.1016/j.techfore.2013.09.016, 2015.

Riahi, K., van Vuuren, D. P., Kriegler, E., Edmonds, J., O'Neill, B. C., Fujimori, S., Bauer, N., Calvin, K., Dellink, R., Fricko, O., Lutz, W., Popp, A., Cuaresma, J. C., KC, S., Leimbach, M., Jiang, L., Kram, T., Rao, S., Emmerling, J., Ebi, K., Hasegawa, T., Havlik, P., Humpenöder, F., Da Silva, L. A., Smith, S., Stehfest, E., Bosetti, V., Eom, J., Gernaat, D., Masui, T., Rogelj, J., Strefler, J., Drouet, L., Krey, V., Luderer, G., Harmsen, M., Takahashi, K., Baumstark, L., Doelman, J. C., Kainuma, M., Klimont, Z., Marangoni, G., Lotze-Campen, H., Obersteiner, M., Tabeau, A. and Tavoni, M.: The Shared Socioeconomic Pathways and their energy, land use, and greenhouse gas emissions implications: An overview, Glob. Environ. Chang., 42, 153–168, doi:10.1016/j.gloenvcha.2016.05.009, 2017.

Rogelj, J., Popp, A., Calvin, K. V., Luderer, G., Emmerling, J., Gernaat, D., Fujimori, S., Strefler, J., Hasegawa, T., Marangoni, G., Krey, V., Kriegler, E., Riahi, K., Van Vuuren, D. P., Doelman, J., Drouet, L., Edmonds, J., Fricko, O., Harmsen, M., Havlík, P., Humpenöder, F., Stehfest, E. and Tavoni, M.: Scenarios towards limiting global mean temperature increase below 1.5 °c, Nat. Clim. Chang., 8(4), 325–332, doi:10.1038/s41558-018-0091-3, 2018.

Rohde, R., Muller, R., Jacobsen, R., Muller, E. and Wickham, C.: A New Estimate of the Average Earth Surface Land Temperature Spanning 1753 to 2011, Geoinformatics Geostatistics An Overv., 01(01), 1–7, doi:10.4172/2327-4581.1000101, 2013.

Rugenstein, M., Bloch-Johnson, J., Gregory, J., Andrews, T., Mauritsen, T., Li, C., Frölicher, T. L., Paynter, D., Danabasoglu, G., Yang, S., Dufresne, J. L., Cao, L., Schmidt, G. A., Abe-Ouchi, A., Geoffroy, O. and Knutti, R.: Equilibrium Climate Sensitivity Estimated by Equilibrating Climate Models, Geophys. Res. Lett., 47(4), 1–12, doi:10.1029/2019GL083898, 2020.

Saji, N. H., Goswami, B. N., Vinayachandran, P. N. and Yamagata, T.: A dipole mode in the tropical Indian ocean, Nature, 401(6751), 360–363, doi:10.1038/43854, 1999.

Saunois, M., Stavert, A., Poulter, B., Bousquet, P., Canadell, J., Jackson, R., Raymond, P., Dlugokencky, E., Houweling, S., Patra, P., Ciais, P., Arora, V., Bastviken, D., Bergamaschi, P., Blake, D., Brailsford, G., Bruhwiler, L., Carlson, K., Carrol, M., Castaldi, S., Chandra, N., Crevoisier, C., Crill, P., Covey, K., Curry, C., Etiope, G., Frankenberg, C., Gedney, N., Hegglin, M., Höglund-Isaksson, L., Hugelius, G., Ishizawa, M., Ito, A., Janssens-Maenhout, G., Jensen, K., Joos, F., Kleinen, T., Krummel, P., Langenfelds, R., Laruelle, G., Liu, L., Machida, T., Maksyutov, S., McDonald, K., McNorton, J., Miller, P., Melton, J., Morino, I., Müller, J., Murguia-Flores, F., Naik, V., Niwa, Y., Noce, S., O'Doherty, S., Parker, R., Peng, C., Peng, S., Peters, G., Prigent, C., Prinn, R., Ramonet, M., Regnier, P., Riley, W., Rosentreter, J., Segers, A., Simpson, I., Shi, H., Smith, S., Steele, L. P., Thornton, B., Tian, H., Tohjima, Y., Tubiello, F., Tsuruta, A., Viovy, N., Voulgarakis, A., Weber, T., van Weele, M., van der Werf, G., Weiss, R., Worthy, D., Wunch, D., Yin, Y., Yoshida, Y., Zhang, W., Zhang, Z., Zhao, Y., Zheng, B., Zhu, Q., Zhu, Q. and Zhuang, Q.: The Global Methane Budget 2000–2017, Earth Syst. Sci. Data, 12(3), 1561–1623, doi:10.5194/essd-12-1561-2020, 2020.

Schiffer, R. A. and Rossow, W. B.: The International Satellite Cloud Climatology Project (ISCCP): The first project of the World Climate Research Programme, Bull. Am. Meteorol. Soc., (76), 779–784, 1983.

Schlesinger, M. E. and Ramankutty, N.: An oscillation in the global climate system of period 65-70 years, Nature, 367, 723–726, 1994.

Schwartz, S. E.: Determination of Earth's Transient and Equilibrium Climate Sensitivities from Observations Over the Twentieth Century: Strong Dependence on Assumed Forcing, Surv. Geophys., 33(3–4), 745–777, doi:10.1007/s10712-012-9180-4, 2012.

Sellar, A. A., Walton, J., Jones, C. G., Wood, R., Abraham, N. L., Andrejczuk, M., Andrews, M. B., Andrews, T., Archibald, A. T., de Mora, L., Dyson, H., Elkington, M., Ellis, R., Florek, P., Good, P., Gohar, L., Haddad, S., Hardiman, S. C., Hogan, E., Iwi, A., Jones, C. D., Johnson, B., Kelley, D. I., Kettleborough, J., Knight, J. R., Köhler, M. O., Kuhlbrodt, T., Liddicoat, S., Linova-Pavlova, I., Mizielinski, M. S., Morgenstern, O., Mulcahy, J., Neininger, E., O'Connor, F. M., Petrie, R., Ridley, J., Rioual, J. C., Roberts, M., Robertson, E., Rumbold, S., Seddon, J., Shepherd, H., Shim, S., Stephens, A., Teixiera, J. C., Tang, Y., Williams, J., Wiltshire, A. and Griffiths, P. T.: Implementation of U.K. Earth System Models for CMIP6, J. Adv. Model. Earth Syst., 12(4), 1–27, doi:10.1029/2019MS001946, 2020.

Shen, Z., Ming, Y. and Held, I. M.: Using the fast impact of anthropogenic aerosols on regional land temperature to constrain aerosol forcing, Sci. Adv., (August), 1–8, 2020.

Sherwood, A. S., Webb, M. J., Annan, J. D., Armour, K. C., Forster, P. M., Hargreaves, J. C., Hegerl, G., Klein, S. A., Marvel, K. D., Rohling, E. J., Watanabe, M., Andrews, T., Braconnot, P., Bretherton, C. S., Foster, G. L., Hausfather, Z., von der Heydt, A. S., Knutti, R., Mauritsen, T., Norris, J. R., Proistosescu, C., Rugenstein, M., Schmidt, G. A. and Tokarska, K. B., Zelinka, M. D.: An assessment of Earth ' s climate sensitivity using multiple lines of evidence, Rev. Geophys., 1–166, 2020.

Shindell, D. T., Lee, Y. and Faluvegi, G.: Climate and health impacts of US emissions reductions consistent with 2 °c, Nat. Clim. Chang., 6(5), 503–507, doi:10.1038/nclimate2935, 2016.

Skeie, R., Berntsen, T., Aldrin, M., Holden, M. and Myhre, G.: Climate sensitivity estimates - Sensitivity to radiative forcing time series and observational data, Earth Syst. Dyn., 9(2), 879–894, doi:10.5194/esd-9-879-2018, 2018.

Smith, S. J. and Bond, T. C.: Two hundred fifty years of aerosols and climate: The end of the age of aerosols, Atmos. Chem. Phys., 14(2), 537–549, doi:10.5194/acp-14-537-2014, 2014.

Smith, T. M., Reynolds, R. W., Peterson, T. C. and Lawrimore, J.: Improvements to NOAA's historical merged land-ocean surface temperature analysis (1880-2006), J. Clim., 21(10), 2283–2296, doi:10.1175/2007JCLI2100.1, 2008.

Solomon, S.: Climate change 2007-the physical science basis: Working group I contribution to the fourth assessment report of the IPCC, Cambridge University Press., 2007.

Stocker, T., Qin, D., Plattner, G., Tignor, M., Allen, S., Boschung, J., Nauels, A., Xia, Y., Bex, V. and Midgely, P.: IPCC, 2013: climate change 2013: The physical science basis. Conribution of working group I to the fifth assessment report of the intergovernmental panel on climate change., Cambridge, UK and New York, NY USA., 2013.

Stouffer, R. J., Yin, J., Gregory, J. M., Dixon, K. W., Spelman, M. J., Hurlin, W., Weaver, A. J., Eby, M., Flato, G. M., Hasumi, H., Hu, A., Jungclaus, J. H., Kamenkovich, I. V., Levermann, A., Montoya, M., Murakami, S., Nawrath, S., Oka, A., Peltier, W. R., Robitaille, D. Y., Sokolov, A., Vettoretti, G. and Weber, S. L.: Investigating the cause of the response of the thermohaline circulation to past and future climage changes, J. Clim., 19(8), 1365–1387, doi:10.1175/JCLI3689.1, 2006.

Swart, N. C., Cole, J. N. S., Kharin, V. V., Lazare, M., Scinocca, J. F., Gillett, N. P., Anstey, J., Arora, V., Christian, J. R., Hanna, S., Jiao, Y., Lee, W. G., Majaess, F., Saenko, O. A., Seiler, C., Seinen, C., Shao, A., Sigmond, M., Solheim, L., Von Salzen, K., Yang, D. and Winter, B.: The Canadian Earth System Model version 5 (CanESM5.0.3), Geosci. Model Dev., 12(11), 4823–4873, doi:10.5194/gmd-12-4823-2019, 2019.

Tatebe, H., Ogura, T., Nitta, T., Komuro, Y., Ogochi, K., Takemura, T., Sudo, K., Sekiguchi, M., Abe, M., Saito, F., Chikira, M., Watanabe, S., Mori, M., Hirota, N., Kawatani, Y., Mochizuki, T., Yoshimura, K., Takata, K., O'Ishi, R., Yamazaki, D., Suzuki, T., Kurogi, M., Kataoka, T., Watanabe, M. and Kimoto, M.: Description and basic evaluation of simulated mean state, internal variability, and climate sensitivity in MIROC6, Geosci. Model Dev., 12(7), 2727–2765, doi:10.5194/gmd-12-2727-2019, 2019.

Taylor, K. E., Stouffer, R. J. and Meehl, G. A.: An overview of CMIP5 and the experiment design, Bull. Am. Meteorol. Soc., 93(4), 485–498, doi:10.1175/BAMS-D-11-00094.1, 2012.

Thomason, L. W., Ernest, N., Millán, L., Rieger, L., Bourassa, A., Vernier, J. P., Manney, G., Luo, B., Arfeuille, F. and Peter, T.: A global space-based stratospheric aerosol climatology: 1979-2016, Earth Syst. Sci. Data, 10(1), 469–492, doi:10.5194/essd-10-469-2018, 2018.

Thompson, D. W. J., Wallace, J. M., Jones, P. D. and Kennedy, J. J.: Identifying signatures of natural climate variability in time series of global-mean surface temperature: Methodology and insights, J. Clim., 22(22), 6120–6141, doi:10.1175/2009JCLI3089.1, 2009.

Tokarska, K. B., Stolpe, M. B., Sippel, S., Fischer, E. M., Smith, C. J., Lehner, F. and Knutti, R.: Past warming trend constrains future warming in CMIP6 models, Sci. Adv., 6(12), 1–13, doi:10.1126/sciadv.aaz9549, 2020.

Trenberth, K. E. and Fasullo, J. T.: An apparent hiatus in global warming?, Earth's Futur., 1, 19–32, doi:10.1002/2013EF000165.Received, 2013.

Vaughan, M. A., Young, S. A., Winker, D. M., Powell, K. A., Omar, A. H., Liu, Z., Hu, Y. and Hostetler, C. A.: Fully automated analysis of space-based lidar data: an overview of the CALIPSO retrieval algorithms and data products, in Proc.SPIE, vol. 5575., 2004.

Volodin, E. and Gritsun, A.: Simulation of observed climate changes in 1850-2014 with climate model INM-CM5, Earth Syst. Dyn., 9(4), 1235–1242, doi:10.5194/esd-9-1235-2018, 2018.

van Vuuren, D. P., Stehfest, E., Gernaat, D. E. H. J., Doelman, J. C., van den Berg, M., Harmsen, M., de Boer, H. S., Bouwman, L. F., Daioglou, V., Edelenbosch, O. Y., Girod, B., Kram, T., Lassaletta, L., Lucas, P. L., van Meijl, H., Müller, C., van Ruijven, B. J., van der Sluis, S. and Tabeau, A.: Energy, land-use and greenhouse gas emissions trajectories under a green growth paradigm, Glob. Environ. Chang., 42, 237–250, doi:10.1016/j.gloenvcha.2016.05.008, 2017.

van Vuuren, D. P., van der Wijst, K.-I., Marsman, S., van den Berg, M., Hof, A. F. and Jones, C. D.: The costs of achieving climate targets and the sources of uncertainty, Nat. Clim. Chang., 10(April), doi:10.1038/s41558-020-0732-1, 2020.

Weaver, C. J., Wu, D. L., Bhartia, P. K., Labow, G. J. and Haffner, D. P.: A long-term cloud albedo data record since 1980 from UV satellite sensors, Remote Sens., 12(12), 1–18, doi:10.3390/rs12121982, 2020.

WMO: World Meteorological Organization, Scientific assessment of ozone depletion: 2018, Glob. Ozone Res. Monit. Proj. #58, 2018.

Wolf, J., Asrar, G. R. and West, T. O.: Revised methane emissions factors and spatially distributed annual carbon fluxes for global livestock, Carbon Balance Manag., 12(1), doi:10.1186/s13021-017-0084-y, 2017.

Wolter, K. and Timlin, M. S.: Monitoring ENSO in COADS with a seasonally adjusted principal component index, Proc 17th Clim. Diagnostics Work., 52–57 [online] Available from: http://www.esrl.noaa.gov/psd/enso/mei/WT1.pdf%5Cnpapers2://publication/uuid/123434A4-48AA-4F4B-A3F7-506504693A80, 1993.

Wolter, K. and Timlin, M. S.: El Niño/Southern Oscillation behaviour since 1871 as diagnosed in an extended multivariate ENSO index (MEI.ext), Int. J. Climatol., 31(7), 1074–1087, doi:10.1002/joc.2336, 2011.

Zelinka, M. D., Myers, T. A., McCoy, D. T., Po-Chedley, S., Caldwell, P. M., Ceppi, P., Klein, S. A. and Taylor, K. E.: Causes of Higher Climate Sensitivity in CMIP6 Models, Geophys. Res. Lett., 47(1), doi:10.1029/2019GL085782, 2020.

Zhang, H.-M., Lawrimore, J., Huang, B., Menne, M. J., Yin, X., Sanchez-Lugo, A., Gleason, B. E., Vose, R., Arndt, D., Rennie, J. J. and Williams, C. N.: Updated Temperature Data Give a Sharper View of Climate Trends, Eos (Washington. DC)., 100, doi:10.1029/2019EO128229, 2019.

Zhang, R. and Delworth, T. L.: Impact of the Atlantic Multidecadal Oscillation on North Pacific climate variability, Geophys. Res. Lett., 34(23), 2–7, doi:10.1029/2007GL031601, 2007.

Zhou, J. and Tung, K. K.: Deducing multidecadal anthropogenic global warming trends using multiple regression analysis, J. Atmos. Sci., 70(1), 3–8, doi:10.1175/JAS-D-12-0208.1, 2013.

Zhu, J., Poulsen, C. J. and Otto-Bliesner, B. L.: High climate sensitivity in CMIP6 model not supported by paleoclimate, Nat. Clim. Chang., 10(5), 378–379, doi:10.1038/s41558-020-0764-6, 2020.

10 Data availability

All data used as inputs into the EM-GC are available from resources on the web. We have provided the links to the resources below. The data are also available along with the EM-GC output data used in this analysis at 10.5281/zenodo.3908407 (McBride et al., 2020) on Zenodo.org.

IOD: The COBE SST data is provided by the NOAA ESRL physical sciences division from their web site https://www.esrl.noaa.gov/psd/.

Tropospheric ozone RF: http://www.pik-potsdam.de/~mmalte/rcps/ .

MEI.v2 and MEI.ext: https://psl.noaa.gov/enso/mei/data/meiv2.data and https://psl.noaa.gov/enso/mei.ext/table.ext.html

PDO: http://research.jisao.washington.edu/pdo/PDO.latest.txt

SAOD: https://eosweb.larc.nasa.gov/project/glossac/glossac

TSI: http://lasp.colorado.edu/home/sorce/data/tsi-data/

OHC Records:

- Balmaseda: http://www.cgd.ucar.edu/cas/catalog/ocean/OHC700m.tar.gz
- Carton: https://www.atmos.umd.edu/~ocean/index_files/soda3_readme.htm
- Cheng: http://159.226.119.60/cheng/
- Ishii: http://159.226.119.60/cheng/
- Levitus: https://www.nodc.noaa.gov/OC5/3M_HEAT_CONTENT/

SSP Database: All information for the SSPs obtained from the SSP database is at https://tntcat.iiasa.ac.at/SspDb/dsd?Action=htmlpage&page=about .

CMIP6 Input Data: https://docs.google.com/document/d/1pU9IiJvPJwRvIgVaSDdJ4O0Jeorv_2ekEtted34K9cA/edit#heading=h.jdoykiw7tpen

CMIP6 Model Output Archive: https://esgf-node.llnl.gov/search/cmip6/